A Decadal Data Set of Global Atmospheric Dust Retrieved From IASI Satellite Measurements

Lieven Clarisse, Cathy Clerbaux, B. Franco, Juliette Hadji-Lazaro, S. Whitburn, A. Kopp, Daniel Hurtmans, Pierre-François Coheur

JGR Atmospheres

RESEARCH ARTICLE
10.1029/2018JD029701

A Decadal Data Set of Global Atmospheric Dust Retrieved From IASI Satellite Measurements

L. Clarisse[1], C. Clerbaux[1,2], B. Franco[1], J. Hadji-Lazaro[2], S. Whitburn[1], A. K. Kopp[1], D. Hurtmans[1], and P.-F. Coheur[1]

[1]Université libre de Bruxelles (ULB), Service de Chimie Quantique et Photophysique, Atmospheric Spectroscopy, Brussels, Belgium, [2]LATMOS/IPSL, Sorbonne Université, UVSQ, CNRS, Paris, France

Key Points:
- A new algorithm for retrieving atmospheric dust optical depth from thermal infrared satellite observations is presented
- Comparisons with AERONET measurements, other satellite measurements, and the ECMWF model are favorable
- Ten years of IASI retrievals are publicly available, and the corresponding seasonal climatology is discussed

Correspondence to:
L. Clarisse,
lclariss@ulb.ac.be

Citation:
Clarisse, L., Clerbaux, C., Franco, B., Hadji-Lazaro, J., Whitburn, S., Kopp, A. K., et al. (2019). A decadal data set of global atmospheric dust retrieved from IASI satellite measurements. *Journal of Geophysical Research: Atmospheres*, *124*, 1618–1647. https://doi.org/10.1029/2018JD029701

Received 22 SEP 2018
Accepted 9 JAN 2019
Accepted article online 14 JAN 2019
Published online 2 FEB 2019

Abstract Aerosol is an important component of the Earth's atmosphere, affecting weather, climate, and diverse elements of the biosphere. Satellite sounders are an essential tool for measuring the highly variable distributions of atmospheric aerosol. Here we present a new algorithm for estimating atmospheric dust optical depths and associated retrieval uncertainties from spectral radiance measurements of the Infrared Atmospheric Sounding Interferometer (IASI). The retrieval is based on the calculation of a dust index and on a neural network trained with synthetic IASI spectra. It has an inherent high sensitivity to dust and efficiently discriminates dust from other aerosols. In particular, over remote dust-free areas, the retrieved levels of optical depth have a low bias. Over sea, noise levels are markedly lower than over land. Performance over deserts is comparable to that of other land surfaces. We use ground-based coarse mode aerosol measurements from the AErosol RObotic NETwork to validate the new product. The overall assessment is favorable, with standard deviations in line with estimated uncertainties, low biases, and high correlation coefficients. However, a systematic relative bias occurs between sites dominated by African and Asian dust sources respectively, likely linked to differences in mineralogy. The retrieval has been performed on over a decade of IASI data, and the resulting data set is now publicly available. We present a global seasonal dust climatology based on this record and compare it with those obtained from independent satellite measurements (Moderate Resolution Imaging Spectroradiometer and a third-party IASI product) and dust optical depth from the ECMWF model.

1. Introduction

Aeolian dust affects the Earth in a multitude of ways. It is an important source of micronutrients for the terrestrial and marine ecosystems but at the same time reduces air quality and visibility in large parts of the world. Mineral dust further plays diverse roles in the Earth's atmosphere, weather, and climate through radiation, cloud, and surface interactions (Boucher, 2015; Knippertz & Stuut, 2014).

Satellite measurements of dust have proven to be very useful in identifying sources (Ginoux et al., 2012), transport (Yu et al., 2013), and relevant meteorological processes (Knippertz & Todd, 2012) and in characterizing diurnal (Schepanski et al., 2009) and seasonal cycles as well as multiyear trends (Zhang & Reid, 2010). In addition, they are now routinely used to evaluate and improve regional and global models (Cuevas et al., 2015) and are assimilated to yield near-real-time forecasts (Benedetti et al., 2009). The most commonly derived aerosol parameter from space is the aerosol optical depth (AOD) at 500/550 nm, which is a measure of how much light is absorbed and scattered by dust at visible wavelengths. A study of 15 different data sets (Carboni et al., 2012), retrieved using a variety of different instruments and algorithms, concluded that agreement of the data sets with ground-based AOD measurements was "reasonably good" but also identified large differences between the different data sets, especially over land. Depending on the sounder and algorithm, other optical (Ångström exponent, single scattering albedo, and even refractive index) and physical (size and shape) parameters can be measured (Tanré et al., 2011).

The most widely used satellite aerosol products are derived from instruments with visible and near-infrared spectral bands, such as Moderate Resolution Imaging Spectroradiometer (MODIS), Advanced Along-Track Scanning Radiometer (AATSR), and POLarization and Directionality of the Earth's Reflectances (POLDER). These are obviously well suited to measure AOD at visible wavelengths. Thermal infrared instruments can also be used to detect and measure dust, but their added value is arguably being underestimated until the

Journal of Geophysical Research: Atmospheres

10.1029/2018JD029701

Table 1
Dust and Volcanic Ash Retrieval Algorithms for AIRS or IASI Radiance Measurements

References	Retrieval	Spectral range	Retrieved dust quantities	Atmosphere (temperature and humidity)	Size distribution	Refractive indices	Surface emissivity	Comments
Capelle et al. (2018) and references therein	Multistage look-up table	26 channels	OD, effective radius, altitude	Retrieved	Lognormal (r_g = 0.79, σ = 1.92)	OPAC, Hess et al. (1998)	Capelle et al. (2012)	
DeSouza-Machado et al. (2006) and DeSouza-Machado et al. (2010)	Spectral fit	36 channels in 800–1,250 cm $^{-1}$ and at ~2,600 cm^{-1}	OD	ECMWF, surface temperature retrieved	Lognormal (σ = 2)	Volz (1973)	Masuda et al., (1988; ocean) and Seemann et al. (2008; land)	Details refer to the 2010 publication
Yao et al. (2012)	Spectral fit	8 channels in 670–972 cm^{-1}	OD, altitude	ECMWF	From in situ measurements, Han et al. (2012)	OPAC, Hess et al. (1998)	Seemann et al. (2008)	
Vandenbussche et al. (2013)	Spectral fit	900–930 cm^{-1} and 1,095–1,125 cm^{-1}	OD, vertical profile	ECMWF/IASI L2	Lognormal (r_g = 0.5, σ = 2.2)	Volz (1972b)	Zhou et al., (2011; land) and Newman et al. (2005; ocean)	
Klüser et al., (2011, 2012)	Singular value decomposition	20 channels in 830–1,250 cm $^{-1}$	OD (altitude)	Not used	Lognormal (multiple from OPAC)	OPAC, Hess et al. (1998) and various minerals	Not used	
Cuesta et al. (2015)	Spectral fit	11 microwindows in 831–1,183 cm^{-1}	OD, vertical profile	ECMWF and retrieved	Lognormal (r_g = 0.92 , σ = 1.75)	OPAC, Hess et al. (1998)	Zhou et al. (2011)	
Ventress et al. (2016)	Spectral fit with a generalized error covariance matrix	680–1,200 cm^{-1}	OD, altitude, and effective radius	ECMWF	Lognormal (σ = 2.0)	Eyjafjallajökull indices		Volcanic ash only
Clarisse et al. (2010) and Newman et al. (2012)	Spectral fit	750–1,250 cm^{-1} or subrange	OD, effective radius	IASI L2	Lognormal (r_g = 0.5, σ = 2.0)	Volz (1973), Balkanski et al. (2007)	Constant	Also applied to other aerosol types
Moxnes et al. (2014)	Look-up table	100 channels in 750–1,250 cm^{-1}	OD, altitude, effective radius	IASI L2	Lognormal (σ = 2.0)	Pollack et al. (1973) and Eyjafjallajökull indices	Constant	Volcanic ash only
Present study	Neural network	100 channels in 750–1,250 cm^{-1}	OD	IASI L2	Lognormal (r_g = 0.5, σ = 2.0)	Volz (1973)	Zhou et al., (2013; land) and Nalli et al. (2008; ocean)	

Note. AIRS = Atmospheric Infrared Sounder; IASI = Infrared Atmospheric Sounding Interferometer; ECMWF = European Centre for Medium-Range Weather Forecasts; OD = optical depth; OPAC = Optical Properties of Aerosols and Clouds.

present day. The inherent advantages of the thermal infrared are however noteworthy; they include the potential to measure in the absence of sunlight (at night or at higher latitudes in the winter), the possibility to differentiate aerosols by composition (e.g., dust, ice, or sulfate aerosols; Clarisse et al., 2013), preferential sensitivity to coarse mode aerosols (Pierangelo et al., 2005), the possibility of retrieving aerosol layer heights (DeSouza-Machado et al., 2010; Pierangelo et al., 2004), and in favorable cases also a size parameter (Pierangelo et al., 2005). Finally, independent measurements over bright surfaces are welcome as their retrieval is not trivial, neither in the visible nor in the infrared. These advantages are all magnified for hyperspectral infrared sounders, even though their higher resolution also brings about a whole set of challenges. Note that in the infrared, the AOD is most naturally retrieved at 10 or 11 μm rather than at visible wavelengths.

Recently, there has been a boom in satellite retrievals of dust (and volcanic ash) from the hyperspectral infrared sounders such as Atmospheric Infrared Sounder (AIRS; Aumann et al., 2003) and Infrared Atmospheric Sounding Interferometer (IASI; Clerbaux et al., 2009). Table 1 lists the currently available retrieval algorithms and some of their defining characteristics. Most of these belong to the category of the physical retrievals that retrieve the parameters of interest by finding a simulated spectrum that matches as close as possible the observed spectrum. This implies finding the minimum of a cost function that, in its most simple form, expresses the distance between the observed and calculated spectrum. The retrievals are therefore guaranteed to be physically compatible with the observed spectrum within a known margin. Physical approaches typically allow a characterization of the uncertainty budget for each individual measurement. Also, a priori information can be added to constrain the retrieval. However, choosing reasonable a priori information for highly variable atmospheric constituents (such as aerosol) is not straightforward.

A subset of the physical retrievals rely on an iterative process: Starting from an initial guess, in each step the retrieval parameters are adjusted and a new simulated spectrum is calculated. In this way, the match with observed spectrum is iteratively improved until convergence is reached. Apart from the main parameters of interest, the retrieval parameters in this approach can include almost any physical parameter (i.e., spectrally interfering trace gases, surface temperature, and surface emissivity). There is however no guarantee that a global optimal solution will be found at the end of the retrieval. Iterative retrievals are also typically slow, in particular those using radiative transfer models relying on line-by-line spectral calculations and that include the effects of multiple scattering in the radiative transfer. Running a forward model for each observation of AIRS or IASI with at least 10^5 cloud-free observations per day involves repeating essentially the same calculations over and over. Such a process has a large degree of redundancy. As an alternative, several physical retrieval schemes rely on look-up tables (LUTs) and avoid this redundancy by running a forward model once to create a library of reference spectra. The algorithm then consists of finding the closest spectral match between a given observed spectrum and the reference spectra. This immediately completes the retrieval, as the reference spectra have known input parameters. The dimensions of a LUT typically include aerosol parameters (abundance, size, and altitude), atmospheric parameters, surface parameters, and the viewing angle. However, as the LUT grows in size, the computational benefits are gradually lost.

The main challenge for the physical retrievals is having a forward model capable of simulating accurate, realistic, and representative high-resolution spectra. Both dust refractive index data and surface emissivity data are variable in space and time, and this requirement is therefore not easily met. Microwindows are often used to focus on the spectral windows that are most sensitive to the retrieval parameters but least affected by those features that are difficult to model. Also, and for the same reason, cost functions other than the simple distance between the calculated and observed spectra have been considered. Peyridieu et al. (2010), for instance, minimize among other things the distance between channel differences rather than the channels themselves. This avoids certain limitations of the forward model or limits the retrieval to reconstruct certain characteristic spectral features. Another approach (Ventress et al., 2016) is to use a generalized error covariance matrix to weigh the distance. This also serves the purpose of reconstructing that part of the spectrum where the sensitivity lies and of taking into account limitations in the forward model. In these more advanced approaches, a full reconstruction of the spectrum is no longer sought or achieved.

Conceptually entirely different are the retrievals based on the construction of an explicit global inverse model, that is, a 1–1 mapping of an input space (spectral information and auxiliary data) to an output space (the physical parameters of interest). We recommend (Aires et al., 2001) for an insightful discussion on the difference between these approaches and the physical retrievals. As an example of such a global inverse

model, Clarisse et al. (2012) built an explicit inverse function for the retrieval of SO_2 column abundances, assuming one high-altitude SO_2 layer, combined with some elementary radiative transfer. Constructing an explicit physically based inversion is, however, for more complex problems impossible. As an alternative, supervised learning techniques allow constructing such an inverse function from a large training set consisting of spectra and matching physical parameters. The inverse function is trained by minimizing a total cost function defined on the entire training data set (Aires et al., 2001).

Artificial neural networks (NNs) are an example of a supervised learning technique. They have become commonplace in remote sensing applications (e.g., Aires et al., 2001; Aires et al., 2002; Blackwell & Chen, 2009; Crevoisier et al., 2009; Hadji-Lazaro et al., 1999; Ioannou et al., 2011; Noia & Hasekamp, 2018; Taylor et al., 2014). In theory they are suited for most retrieval problems, as NNs can approximate arbitrarily close any continuous function on compact input spaces. In this paper, we present a new dust optical depth (DOD) retrieval for IASI observations based on NNs.

The most important element in supervised learning is the training set, which for remote sensing applications can be acquired in two distinct ways. The most straightforward approach is to use a set of real observed spectra, matching auxiliary data, and collocated output data. This is the ideal case, as the input data are then fully representative for real data. In this case, the output data has to be obtained from an alternative retrieval method or a third party source and might be subject to serious errors or biases. For the present retrieval which is focused on DOD at 10 μm, no such third party data are available. The choice was therefore made to build the training set from synthetic spectra, for which the output data (or thus input data in the forward model) are known without error. In this perspective, the NN is an alternative to performing a LUT retrieval. However, NNs are more flexible. For instance, they remain more manageable for larger input spaces, as a LUT grows exponentially with the number of input parameters. With a synthetic training database, the main challenge is to avoid errors or misrepresentations in the forward model. As pointed out above, this is also an issue in most other retrieval approaches. It might even be more important for NN approaches, which can behave completely unpredictable when faced with data that is for instance systematically offset with respect to the training set. Another issue is the treatment of instrumental noise. To get a well-behaved retrieval, both these issues need to be addressed very carefully.

To reduce the dependency on the forward model in the present retrieval approach, the spectral input is limited to two parameters, making the NN also more robust and less sensitive to overtraining (Aires et al., 2002). The features are a dust index and a baseline temperature. Assuming knowledge of appropriate auxiliary data, as will be shown in section 3.3, these two spectral parameters hold enough information to retrieve the DOD.

Consider a dust index defined as the surface area of the "V"-shaped extinction in the spectrum in the 800–1,200 cm^{-1} range in brightness temperature space (DeSouza-Machado et al., 2006). Such an index quantifies the overall broadband extinction, and a NN trained on this input parameter, rather than a series of individual spectral channels, would be relatively robust against inaccuracies in the forward model (such as inaccuracies in the refractive index data or the surface emissivity data). This example illustrates the advantages of using a single quantity that characterizes the overall spectral extinction due to dust in the infrared. The index employed in the present study is more difficult to visualize but fulfills the same role. It is based on statistical information of observed IASI spectra and has already proven to be very powerful in several studies on the detection of trace gases and aerosols (see references below). By training our NN with this input parameter, which carries the information on the strength of the dust spectral extinction, we expect our retrieval to be relatively insensitive to inaccuracies in the forward model but at the same time to have a high signal-to-noise ratio. Working with this (noisy) index also allows treating the instrumental noise in a natural way.

Following the development of the dust NN retrieval algorithm presented in this paper (v8 is described here, v1 dates back to 2015), it was also found to be easily adaptable to the retrieval of trace gases. In Whitburn et al. (2016) and Van Damme et al. (2017) it was for instance shown that the method works well for the retrieval of NH_3 and that the approach offers a number of important advantages over other schemes. Very recently, the method was also applied to the retrieval of several volatile organic compounds.

This paper is organized as follows. In the next section, the dust index is introduced and examples of its dependence on other parameters, such as altitude and DOD, is given. Section 3 describes the setup and training

of the NN. Here we also detail the forward model that was used to build the training set. Even though the overall retrieval scheme was developed to reduce its impact, best effort has been made to make the forward model as accurate as possible. The actual retrieval, including prefiltering and postfiltering and derivation of uncertainty estimates is provided in section 4. In section 5 the performance of the new retrieval is evaluated via comparison with ground-based AErosol RObotic NETwork (AERONET) observations, independent satellite measurements, and a model. We end with a summary and directions for future work.

2. A Dust Index

2.1. Definition

The dust index used in this study is defined as

$$R = \frac{K^{\mathrm{T}} S^{-1}(y - \bar{y})}{\sqrt{K^{\mathrm{T}} S^{-1} K}}, \tag{1}$$

with y the observed spectrum and K a Jacobian with respect to DOD. The constants $\bar{y}$ and S are respectively the mean and associated covariance matrix of a representative set of spectra without an observable dust signature. Equation (1) can be derived from the weighted least squares estimate (i.e., the maximum likelihood solution; Walker et al., 2011) or from linear discrimination analysis (Clarisse et al., 2013); we refer to these papers for a detailed account on the background and interpretation of the index R. In essence, it quantifies the magnitude of the spectral dust signature as the weighted projection of a dust Jacobian onto the observed spectrum. The weights are provided by the inverse of the covariance matrix, which optimally weighs in the expected (dust-free) variability and correlations of all spectrally interfering parameters. This weighing becomes particularly powerful when dealing with high-resolution spectra and for the detection of signatures over a broad spectral range. The denominator and the term $\bar{y}$ are optional but very convenient as they center and normalize the index so that on dust-free spectra, the mean is 0 and the standard deviation 1. Larger values indicate the presence of dust, and for a spectrum with an R above 2 or 3 "standard deviations" dust can be assumed to be present in the observed scene. By imposing a suitable threshold, this index can thus be used as a dust detection flag.

No forward model is needed at all in the calculation of the index, as both the covariance matrix and Jacobian can be built from actual observed IASI spectra, as detailed in the next section. This makes the index even more appealing and powerful, as forward models can never perfectly reproduce real spectra, in particularly when it comes to reproducing aerosol signatures observed in high-resolution spectra (Clarisse et al., 2010; Clarisse et al., 2013).

2.2. Construction

We now provide further details on the determination of the constants $\bar{y}$, S, and K in equation (1). The same 100 spectral IASI channels were used as in Clarisse et al. (2013). These channels represent the brightest channels (on average) per 5-cm^{-1} interval in the range 755–1,250 cm^{-1} and contain most of the available spectral information on the broadband extinction of dust aerosols.

The background (dust-free) $\bar{y}$ and corresponding S were determined from global IASI data of the year 2013 (3 days per month). In Clarisse et al. (2013), they were determined via an iterative approach, where in each iteration the detection of dust is improved, which leads to a better definition of these same constants in the next iteration. The disadvantage of such an approach is that it can be sensitive to the choice of dust detection method in the first iteration and to the specific detection thresholds that are used in each step. In the present study, we found a way of generating the mean background and covariance that is easier and also more readily adaptable to other instruments. Namely, we used modeled DOD runs from the ECMWF model (Benedetti et al., 2009; Morcrette et al., 2009) to remove spectra potentially affected by dust using a threshold of 0.1 on the day average of the DOD at 550 nm. In the second iteration, observations were removed with an R value above 3 (ocean) and above 2 (land) in addition to those with a modeled DOD of 0.2 over land. This second iteration turned out to be as performant as the original approach that relied on an ad hoc first dust detection and many iterations. Several other improvements were introduced with respect to Clarisse et al. (2013). First, only cloud-free observations were considered, as the actual DOD retrieval is designed for cloud-free observations. This alone helps to improve the dust detection over cloud-free scenes as the covariance matrix expresses better the variability of these observations. A cloud coverage of 10% was used as a threshold to keep only the clearest pixels; cloud information was taken from the IASI L2 version 6 product

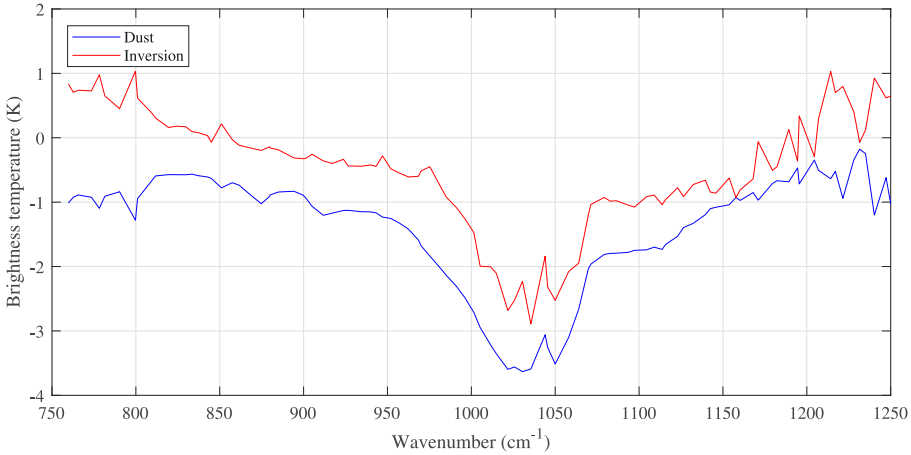

Figure 1. The IASI-derived Jacobian used for dust detection (blue) together with the Jacobian used for the removal of false detection due to large temperature inversions (red). The spectra shown have a reduced sampling of 100 channels. IASI = Infrared Atmospheric Sounding Interferometer.

(August et al., 2012). Second, and for the same reason, separate $\bar{y}$ and S quantities were calculated for ocean and land. We considered that the increase in sensitivity warrants the added complexity. Third, while IASI spectra were chosen randomly, their latitudinal distribution was altered to be uniform in terms of spatial coverage, in order to compensate for the polar orbit which provides a relatively much larger coverage of the poles than of the tropical latitudes. Finally, it was decided to also exclude observations over snow and ice surfaces. These were removed using a monthly climatology built from ERA ECMWF reanalyzed data (Dee et al., 2011) of ice and snow cover with some manual adjustments. Threshold values of 30% of sea ice or 2-cm snow were used. These four changes help to optimize the index for the target observations, namely, for cloud-free midlatitudinal and tropical observations.

In the paper Clarisse et al. (2013) on aerosol detection, 11 different Jacobians were used in the dust detection scheme. The reason for using more than one class was to account for the variability in the observed dust signatures. Jacobians were calculated as $K_r = \bar{y} - y_r$, with y_r the average dust spectrum for each of the 11 classes. Defined as such, they can contain large contributions from differences in surface temperature and ozone abundance (which absorbs in the same spectral range). While these contributions are largely canceled out when weighing K_r with the inverse of the covariance matrix, there was some dependence of the index on the surface temperature. For this reason we calculated here Jacobians as the average difference between spectra with a large spectral signature due to dust ($R > 6$) and those with a weaker signature ($R > 1$ and $R < 3$) over small geographical regions and time periods. Such Jacobians represent mostly the variations in DOD alone. To simplify further processing in the NN, a single Jacobian was sought, for which the detection was satisfactory both over ocean and over land. Therefore, among the many different Jacobians that were generated, one particular one, shown in Figure 1, was selected that resulted in a detection that was globally satisfactory and almost equivalent with the approach that used several classes. The Jacobian was calculated from spectra observed over Morocco in June 2013.

2.3. Biases Over Deserts

A dust index constructed following the above approach suffers from false detections and biases over deserts. This became apparent in a first version of the retrieval algorithm where specific areas over deserts showed enhanced columns throughout the year, clearly attributable to localized surface emissivity effects in the thermal infrared. Surface emissivity is spatially too heterogeneous to be completely accounted for in one fixed global covariance matrix (the index is only unbiased if the underlying statistics are Gaussian). Although the biases are not that large, it is relatively straightforward to make a first-order correction by estimating the spatially variable biases from a period in the year (usually the winter) when IASI sees almost no or practically no airborne dust. This assumes that the emissivity and corresponding bias is constant throughout the year (or at the least has less variability than the bias itself). As the biases only occur over deserts, we first identified desert areas from a threshold of 0.94 on the mean infrared emissivity between 800 and 1,230 cm^{-1} (Zhou et al., 2013). Next, for each of the identified regions, the month was selected with the least amount

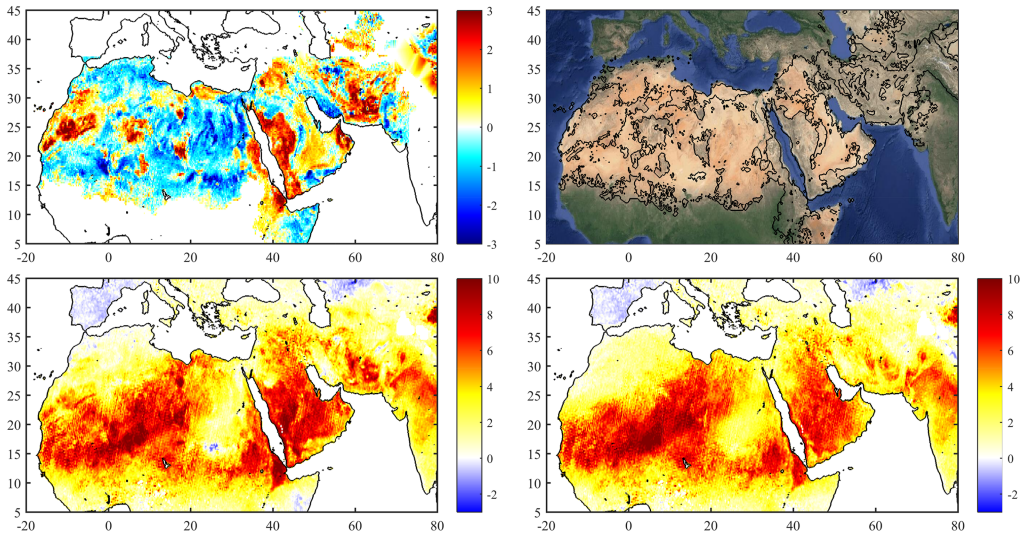

Figure 2. Bias correction of the dust index R (equation (1)) over deserts. The top left panel shows the observed bias over the (area-dependent) months where little or no detectable dust is expected. The top right panel is a visible map; the superimposed black line delineates the sign changes in the bias (thus corresponding to the transition from yellow to blue in the first panel). The bottom panels show respectively the uncorrected and corrected gridded May 2013 average of the R value over land.

of expected airborne dust, using a first version of the retrieval algorithm and output of the ECMWF model (Benedetti et al., 2009; Morcrette et al., 2009). These months are either November, December, or January in the Northern Hemisphere and May or June in the Southern Hemisphere. The average R values for the selected months were then gathered on a single $0.25° \times 0.25°$ grid. This grid constitutes the assumed bias and is used to debias all the R data. Figure 2 illustrates this bias correction for northern Africa and the Middle East. The top left panel shows the calculated bias. On the top right a visible map is shown. The superimposed contour delineates where the bias changes sign; it is clear that these transitions correspond to changes in surface type (rocky soils typically exhibit a positive bias and sandy soils a negative bias). The bottom panels illustrate the bias correction on May 2013. The bottom left panel shows an uncorrected average of R values, where despite the change of color scale, some of the features in the top panels can still be recognized. The average of the debiased R values is shown on the bottom right and is visibly smoother than the left panel.

2.4. Biases Over Coastal Areas

Unexpected enhancements in the dust index were also observed over certain coastal areas, for example, off the coast of California. This was mostly the case in the warmer seasons and is due to temperature inversions, which off the coast of California are caused by high-pressure systems that warm the free troposphere by subsidence. For some individual cases, these inversions can be as large as 15 K. From a radiative transfer point of view, an inversion entails that some of the usual spectral features due to water vapor in the 750–1,250 cm^{-1} spectral range are observed in emission rather than absorption. The resulting shape of the baseline of the spectrum in brightness temperature space resembles the V-shaped extinction, characteristic for dust, which explains the observed biases. An "inversion" Jacobian obtained from the difference of such spectra dur-

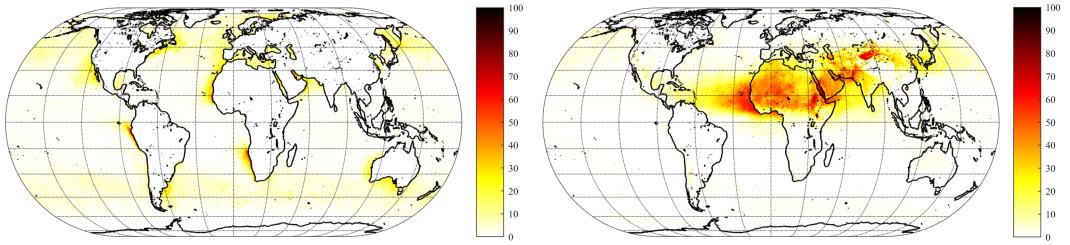

Figure 3. Percentage of cloud-free daytime observations in 2013 that are removed as they are potentially affected by temperature inversions (left panel), and the percentage of remaining observations detected as dust (right panel).

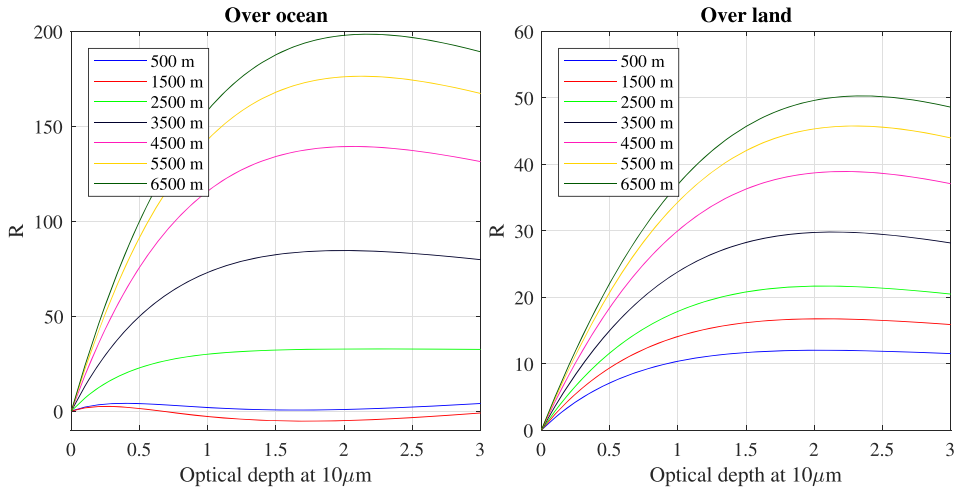

Figure 4. Dependence of the *R* value on altitude and dust optical depth for (left) an ocean and (right) a land scene.

ing June 2013 off the coasts of Quebec is shown in Figure 1. The resemblance with the dust Jacobian is obvious; observe also the presence of absorption features in the dust Jacobian and emission features in the inversion Jacobian.

As the associated biases are variable, there is no straightforward correction available. For this reason, affected observations are filtered out from further processing using a dedicated flag. This flag is setup similarly as the dust detection flag, and an R_{inv} value is calculated with the inversion Jacobian. Whenever R_{inv} exceeded a value of 2 and the dust *R* value, the observation is considered to be dominated by this inversion effect and is excluded from further processing. The fraction of these on the total number of cloud-free observations is shown in Figure 3 for the year 2013 (left panel). The fraction of dust detections over the remaining observations is shown on the right. Dust detection thresholds of 2 and 3 were applied respectively over ocean and land.

The number of observations disregarded in this way is rather large (e.g., $\sim$ 10% over a large part of the oceans in the Northern Hemisphere), but it should be stressed that this filtering determines only what pixels are processed further on and does not alter the actual retrieval. The filter also removes some cloud-contaminated pixels that are not flagged as such in the Eumetsat L2 data. Unfortunately, also some pixels that likely contain observable quantities of dust are removed, in particular close to the west coast of Africa, the northern part of the Red Sea, and the Persian Gulf. The retrieval algorithm relies on the fact that the *R* value is mostly a measure of the spectral signature of dust alone, so that in the current setup this filtering procedure is needed. For the end product, the main consequence is that these regions will have less coverage than other nearby regions. It is one area of the algorithm that should be improved in future work.

2.5. Dependencies

The *R* value quantifies the magnitude of the dust signature in the observed spectra. As such, it is correlated with dust load but also with the dust altitude. The dependence of the *R* value on the DOD and the altitude is illustrated in Figure 4 for an ocean and a land scene and a dust plume of 1-km thickness. For DOD below 0.5, there is an almost linear relation between the DOD and the index. Above DOD of around 2, the index saturates and eventually even decreases. This is a consequence of the fact that for such large DOD the V-shape flattens out. The dependence with altitude is a clear manifestation of thermal contrast. Higher altitudes correspond to colder temperatures and hence larger temperature differences with the surface, which result in a better sensitivity to dust. For the selected ocean scene, the lowermost layers have negligible thermal contrast and close to zero sensitivity.

The rest of the retrieval algorithm is designed to convert the dust index into an DOD, by taking into account the main dependencies. A similar idea was already applied in Van Damme et al. (2014) and Bauduin et al. (2016) for NH_3 and SO_2, respectively. In those studies, LUTs were used for the conversion. Here a more flexible NN is used instead.

Table 2
Measured and Calculated Refractive Index Data of Dust and Sand in the Thermal Infrared

Description	Range (cm^{-1})	References and comments
Measurements		
Dust from precipitation (midlatitude rained out mixtures of soil particles, fly ash/soot and pollen)	250–50,000	Volz (1972b), samples described in Volz (1972a), tabulated in D'Almeida et al. (1991); Shettle and Fenn (1979); World Meteorological Organization (1986); and referred to as "dust-like"; termed "insoluble" in Koepke et al. (1997) and Hess et al. (1998)
Midlatitude dust	333–4,000	Volz (1983), two size classes
Saharan dust, Niamey, Niger	250–4.000	Fouquart et al. (1984, 1987)
Saharan sand, Barbados, West Indies	250–4,000	Volz, (1973, figure)
Saharan sand, Mauritania, dry and 50% relative humidity	470–6,980	ARIA (2017) measurements made by D. Peters
Afghanistan, Tadzhikstan sand	400–4,000	Sokolik et al., (1993, 1998)
Negev, Israel clean and dust storm	833–1,333	Fischer (1976) (see also Sokolik et al., 1998)
Dust in Southwest United States, Texas	625–1,000	Patterson (1981), imaginary part only; real part calculated and shown in Sokolik et al. (1998)
Niger, Algeria, Tunisia, and the Gobi desert	400–4,000	Di Biagio, Boucher, et al. (2014) and Di Biagio, Formenti, et al. (2014)
9 different global dust source areas (19 samples)	666–3,333	Di Biagio et al. (2017)
Mixtures		
GADS/OPAC mineral component	250–4,000	Koepke et al. (1997) and Hess et al. (1998); Mainly Volz (1973) with addition of extra quartz absorption features
Mixture of hematite and quartz; hematite is 10% by volume	33–50,000	Longtin (1988)
Composite clay (1/3 by weight of montmorillonite, illite, and kaolinite)	50–4,000	Querry (1987)
Composite of hematite, illite, montmorillonite, quartz, kaolinite, and calcite	100–34,722	Balkanski et al. (2007)

Note. Most data can be found in the HITRAN (Massie & Hervig, 2013), GEISA (Jacquinet-Husson et al., 2016), and ARIA (ARIA, 2017) spectral databases. OPAC = Optical Properties of Aerosols and Clouds; GADS = Global Aerosol Data Set; HITRAN = HIgh Resolution TRANsmission molecular absoption database; GEISA = Gestion et Etude des Informations Spectroscopiques Atmosphériques.

3. Training the NN

3.1. The Forward Model

The forward model code that was employed for the generation of the training data set is called Atmosphit (Coheur et al., 2005; Clarisse et al., 2010). It is a line-by-line code which uses the doubling-adding method for its radiative transfer and for dealing with the effects of multiple scattering. For aerosols, the absorption, scattering coefficients, phase function, and asymmetry parameters are calculated using Mie scattering.

The particle size distribution for the dust particles was assumed lognormal, with a geometric standard deviation of 2 and a geometric mean radius of 0.5 μm. This is similar to the mineral-transported aerosol component in the OPAC model (Hess et al., 1998; although they use 2.2 for the standard deviation) and to what is used in other retrieval schemes (see Table 1). With an effective radius of 1.66 μm, this distribution can be considered to be a coarse mode distribution, even when most of the particles are in the accumulation mode (smaller than 1 μm). While dust particle size distributions can vary greatly in space and time (Mahowald et al., 2014; Reid et al., 2003), the effect of the size distribution on the retrieved DOD has been shown to be

of second-order importance (Capelle et al., 2014; Vandenbussche et al., 2013), and hence we have neither considered other size distributions nor attempted to retrieve an effective radius.

Table 2 gives an overview of the measured or synthesized refractive index data of dust and sand that are available in the thermal infrared. To decide which refractive index should be used for producing the training data set, we performed a retrieval experiment. For this, IASI spectra with a strong dust signature were selected over the Atlantic ocean. Ocean scenes were chosen as the surface emissivity is much better constrained over ocean than over land. A spectral fit, along the lines of Clarisse et al. (2010), was performed over the range 750–1,250 cm^{-1} with seven different refractive index data sets: Niamey dust (Niger; Fouquart et al., 1984), Tamanrasset sand (Algeria) N32/N93 (Di Biagio, Boucher, et al., 2014), Mauritania sand (ARIA, 2017), midlatitude rained out dust (Volz, 1972a), GADS/OPAC mineral (Hess et al., 1998), and finally Saharan sand collected at Barbados, West Indies (Volz, 1973). The Barbados and Mauritania refractive indices consistently provided the best fits, and in the end we settled on the Barbados data as it is also the most widely used. This experiment was performed before Di Biagio et al. (2017) published their unparalleled data set of 19 soil-derived mineral dust aerosols, which are representative for dust transported over short to medium distances (1–2 days). No doubt that using those would have been better for the simulation of spectra over land (see in this context also; Liuzzi et al., 2017). Using a LUT approach, Capelle et al. (2014) estimated differences up to 25% in the retrieved DOD for different sets of refractive indices. They based this estimate on large differences found in the simulation of individual spectral channels. Our R index which depends on the entire thermal infrared window quantifies the integrated extinction signature and so in principle should be less affected by high frequency features in the refractive index data. However, selecting more representative refractive indices over land and ocean would improve the representativeness of the training data set, and it is therefore an area of the algorithm where further improvement is possible or for which in the future the effects of choosing one particular data set over another should be quantified.

For modeling the vertical distribution of dust aerosols, we assumed that each atmosphere contained a single sand layer within the 0- to 7-km range. Following the 1-km resolution of the atmospheric layering in the radiative transfer model below 10 km, this resulted in seven possible layers of 1-km thickness: 0–1, 1–2, 2–3, 3–4, 4–5, 5–6, or 6–7 km. While, as shown in the previous section, the radiative transfer in the infrared is very sensitive to the assumed mean altitude of the layer, layer thickness is known to have little impact (Peyridieu et al., 2010). We verified this on selected atmospheres with a small simulation experiment where the 1-km layering in the radiative transfer simulation was replaced with a 250-m layering and with dust confined to be within a layer of 250-m thickness. Differences in the dust absorption signature were found to be no larger than 1%. This confirms that infrared sounders have little or no sensitivity to layer thickness below a certain threshold and also shows that the 1-km layering used in the radiative transfer is sufficiently resolved for our purposes.

For accurately modeling the surface radiation over land, the high-resolution surface emissivity database of Zhou et al., (2011, 2013) was used. This database provides monthly averaged emissivity data, but we only used the November data, as close inspection led us to conclude that there is residual aerosol contamination in the Northern Hemispheric summer data. For the water surface emissivity, we used the data from Nalli et al. (2008) at a wind speed of 6 m/s.

3.2. Training Data Set

The starting point for the training data set is a collection of randomly selected observations of IASI for the year 2013 (over $2 \cdot 10^5$ observations in total). It is not the IASI spectra that are of interest here but their corresponding L2 data (i.e., pressure, temperature, ozone, and humidity profiles and surface temperature) as these are used to define a representative set of atmospheres. As the same type of L2 data will be used as part of the input for the NN retrieval, this guarantees that this aspect of the training set is fully representative for its future input. The selection of these observations was random but made in such a way that 90% of the observations were flagged as containing dust by the dust detection algorithm. This guarantees that the training set contains enough relevant training data and furthermore this makes the network perform best where it really matters (as low DOD scenes can afford a larger relative error). DOD and mean layer altitudes were chosen at random, respectively between 0 and 3 and between 0.5 and 6.5 km. For each simulated spectra, an accompanying spectra without aerosol was generated as well. This was done to remove any possible R-biases caused by the forward model (by subtracting the R value of the aerosol-free spectra from the R value of the aerosol spectra).

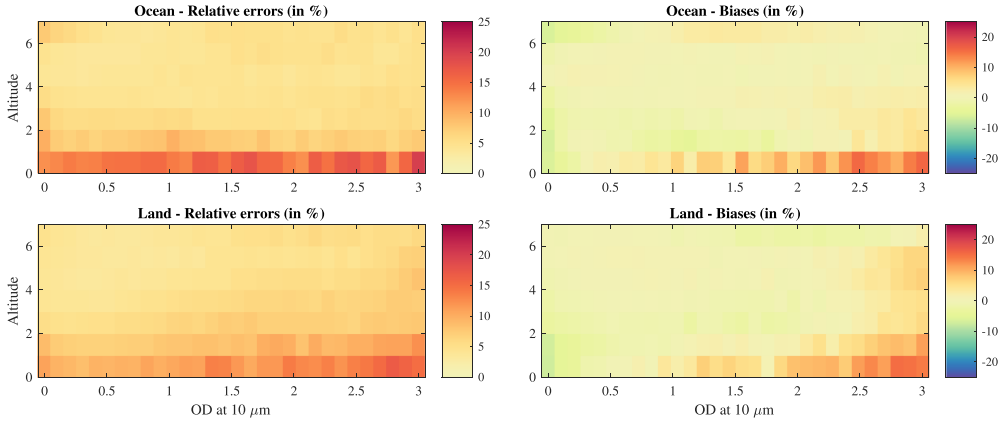

Figure 5. Performance of the neural network on the training data set, in terms of relative errors and biases and as a function of OD and altitude. OD = optical depth.

3.3. NN Setup

The main parameter of interest is the DOD at 10 μm. However, for reasons we will now explain, the NN was setup to calculate a conversion ratio (CR) by which the R value should be multiplied to get the DOD, that is, DOD $= R \times$ CR (see also the related discussion in Whitburn et al., 2016). For given atmospheric conditions, this CR is constant for low DOD as the DOD and the R value are then linearly dependent (see Figure 4). Retrieving a CR rather than the DOD has important implications on how the retrieval deals with the instrumental noise, especially when the DOD is low. Neglecting possible biases, the R is composed of two components, one due to random instrumental noise and one due to the actual dust contribution: $R = R_{\text{noise}} + R_{\text{dust}}$. As we have pointed out before, R_{noise} is distributed normally with a mean of 0 and a standard deviation of 1. R_{dust} can be very small compared to R_{noise} in case of low DOD or low sensitivity. In these cases, we have OD $\approx R_{\text{noise}} \times$ CR, and thus we observe that the retrieved DOD, in absence of observable amounts of dust, is by design normally distributed with a mean of 0. This also implies that also negative DODs will be retrieved. The use of negative DODs is not new: They can for instance be found in MODIS AOD data starting from the Collection 5 (Levy et al., 2007, 2013). In the first of these papers the authors call negative OD "statistically imperative" for creating a unbiased data set. For IASI observations of DOD, which are expected to be measurable only in part of the data (i.e., in large areas and or time periods, the OD retrieval should average to 0), the necessity of having negative OD retrievals for an unbiased product becomes even more important. So our retrieval setup deals automatically and in a natural way with the instrumental noise: An unbiased product is guaranteed, and the NN does not need to worry about instrumental noise (but see below) and can assume that the measurements are noise-free.

The CR depends on a number of parameters, which for an accurate retrieval should all be part of the input data of the NN. The first one is the R value itself, as the linearity between the DOD and the R value only holds for low DODs. The satellite viewing angle directly influences the path length and hence the observed dust signature and R value; it is therefore included as an input parameter. Another important parameter is the temperature of the dust layer (see Figure 4 and the related discussion). The surface temperature is the fourth main parameter affecting the radiative transfer. While it is available as an official IASI L2 product, it is known to have larger uncertainties in the presence of aerosols. It is probably only retrievable accurately by simultaneously retrieving the DOD. Instead of the surface temperature, we therefore feed the network with three additional parameters: (i) the R value itself (already included), (ii) a "baseline temperature," obtained as the average brightness temperature in the channels at 801 and 809.75 cm^{-1}, and (iii) the mean surface emissivity at those channels. The selected channels provide information on the underlying surface temperature for low to medium DOD. This guarantees that the NN has enough information to work out the radiative transfer of the problem. The remaining input parameters are five partial columns of water vapor (0–1, 1–2, 2–3, 3–5, and 5–7 km), the ground surface pressure, and the altitude of the dust plume in kilometers. The latter was included to give the NN information on the water vapor amount below and above the plume.

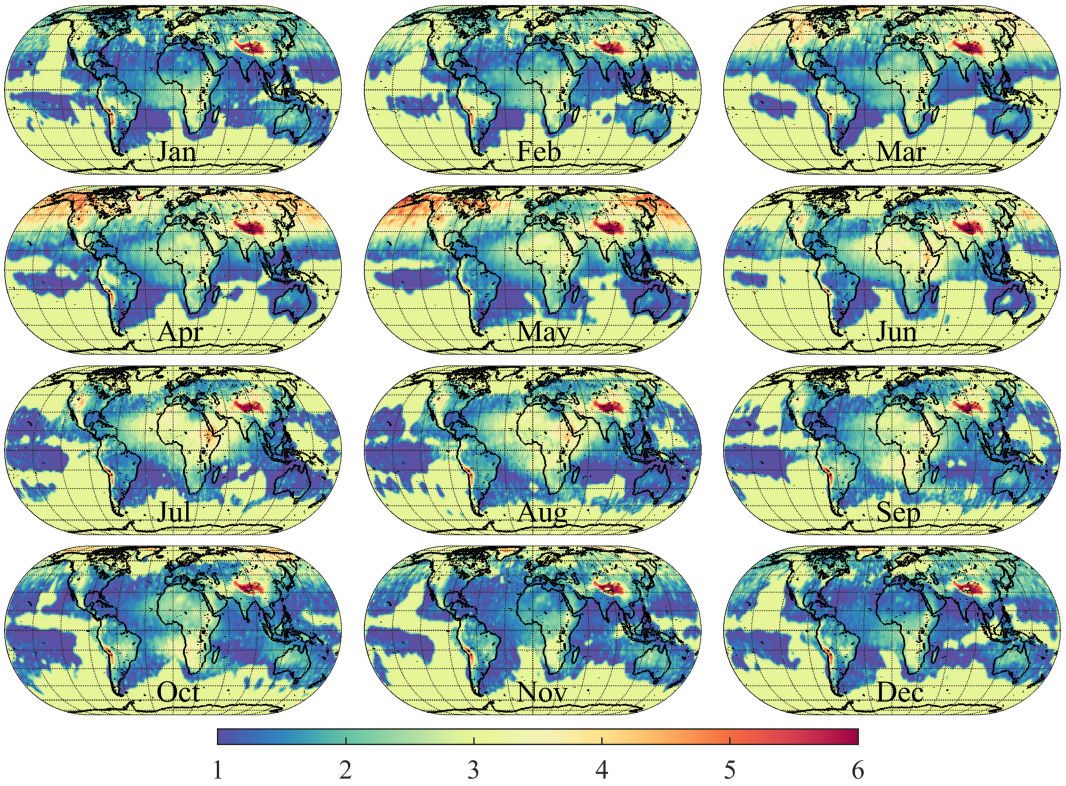

Figure 6. Dust altitude climatology (in km) derived from Cloud-Aerosol Lidar and Infrared Pathfinder Satellite Observation data.

When there is little or no sensitivity to dust, the CR can reach very large values, rendering the network untrainable. To counter this, observations for which the CR exceeded a value of 0.3 over land and 0.1 over ocean were removed from the training data set.

The network itself is a feed-forward network with 12 inputs and 1 output (defined above), two hidden layers with five nodes each and one output layer. The transfer function for the hidden layers is tanh, while the linear transfer function is used for the output layer. Separate networks were setup for ocean and land, as their R values depend on different covariance matrices.

3.4. Training Performance

The network as defined above has a total of 101 tunable parameters. These were obtained via Levenberg-Marquardt back propagation on the training data set. The network was setup and trained using Matlab's NN toolbox. Prior to training, noise was added to the R value to make the network more robust (since the noise can several times exceed its actual value). Note, though, that the main dependency on the noise is already taken care of by training on the CR rather than on the DOD.

The training performance is summarized in Figure 5 in terms of mean relative errors and biases on the OD, and as a function of OD and altitude. For the calculation of the OD via OD = $R\times$ CR, R was assumed to be noise-free. The relative errors are calculated as the mean of the absolute value of the relative errors for all the observations in a given altitude-OD bin. They are of the order of 10%, except at the lowest altitudes, where they reach 25%. The biases are calculated as the mean of the relative errors. They are mostly close to 0, with a few exceptions again for low altitude. In practice, the uncertainties on all input parameters will lead to larger uncertainties in the retrieved DOD than the training performance suggests. These will be considered and discussed in section 4.3.

4. Running the NN

4.1. Input Data and Prefiltering

All the input data are taken directly from the IASI L1C or L2 data, except for the dust altitude. While future versions of the algorithm might attempt to retrieve this parameter, at present a monthly climatology of dust

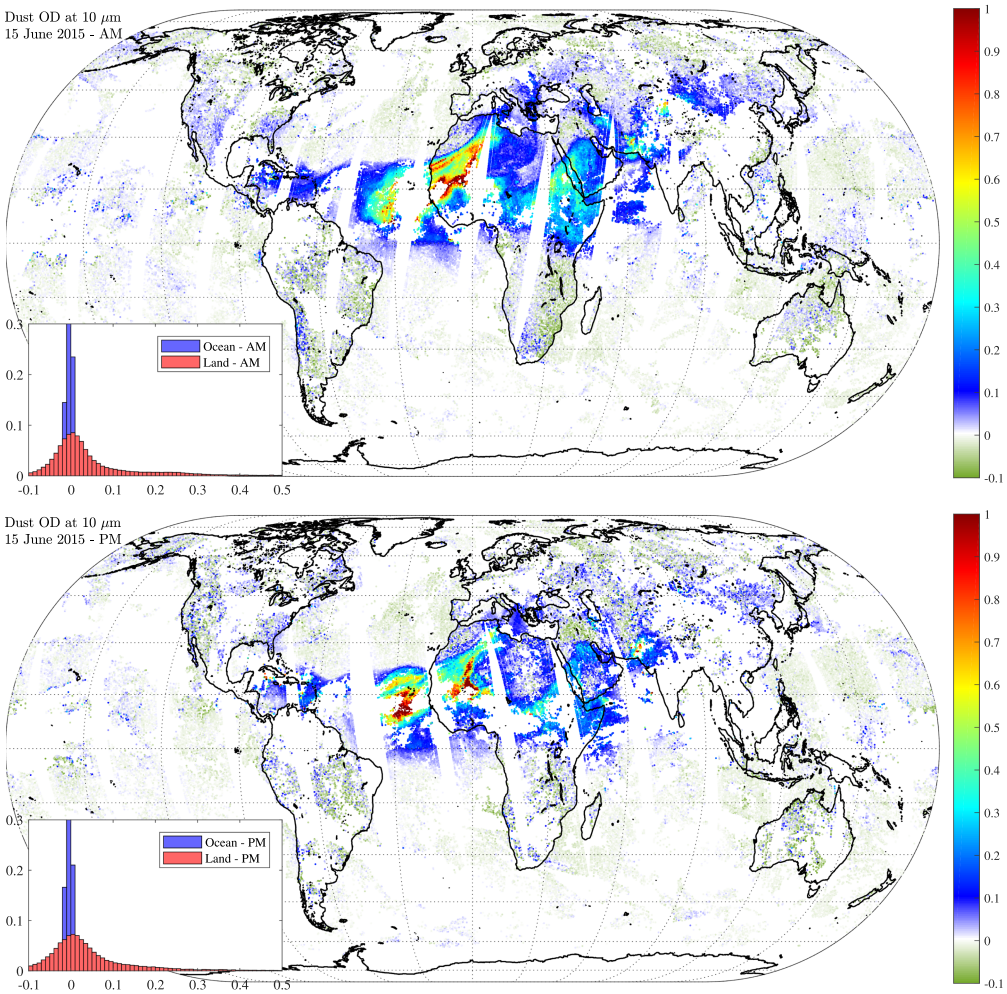

Figure 7. IASI-retrieved DOD for 15 June 2015 for the morning (top) and evening (bottom) overpass. The insets show the probability histograms of the retrieved values over the entire globe. IASI = Infrared Atmospheric Sounding Interferometer; DOD = dust optical depth.

altitudes is used. This climatology was built from the Cloud-Aerosol Lidar and Infrared Pathfinder Satellite Observation 5-km Aerosol Layer product (v4.10; Winker, 2016; Winker et al., 2009, 2013) for all available data in the period 2006–2016. Similar climatologies were calculated and analyzed in Yu et al. (2010), Tsamalis et al. (2013), and Huang et al. (2015). Here the climatology was obtained as follows. First all the layers were selected that are classified as "dust," "polluted dust," or "dusty marine," and for which the feature type quality assessment is high and for which the cloud/aerosol/polar stratospheric cloud type quality assessment is confident. To remove noise, only layers below 7 km were considered. Next, considering a 1° × 1° grid, the mean and standard deviations of the layer altitudes were calculated (the altitude for an individual layer was obtained by averaging the layer top and layer base). Finally, grid boxes for which less than fifty measurements were obtained, were assigned a standard deviation of 2 and a mean of 3 km. As a result, a 1° × 1° monthly dust altitude climatology is obtained consisting of a mean altitude (shown in Figure 6) and corresponding standard deviation. Prior to running the network, the observations undergo a prefiltering operation that selects all spectra for which the retrieval should be performed. The same criteria apply as those for the dust detection algorithm; that is, spectra are retained only if they have (i) a cloud coverage below 10%, (ii) no (climatological) snow or ice coverage, and (iii) no detected inversions.

4.2. An Example

Retrievals for 15 June 2015 are shown in Figure 7 for the morning (top) and evening (bottom) overpass. Gaps in the coverage are mostly due to clouds but also due to the other prefilters (see section 4.1) and post-filters (see section 4.3). Enhancements are observed where they are expected, that is, over land: Middle East,

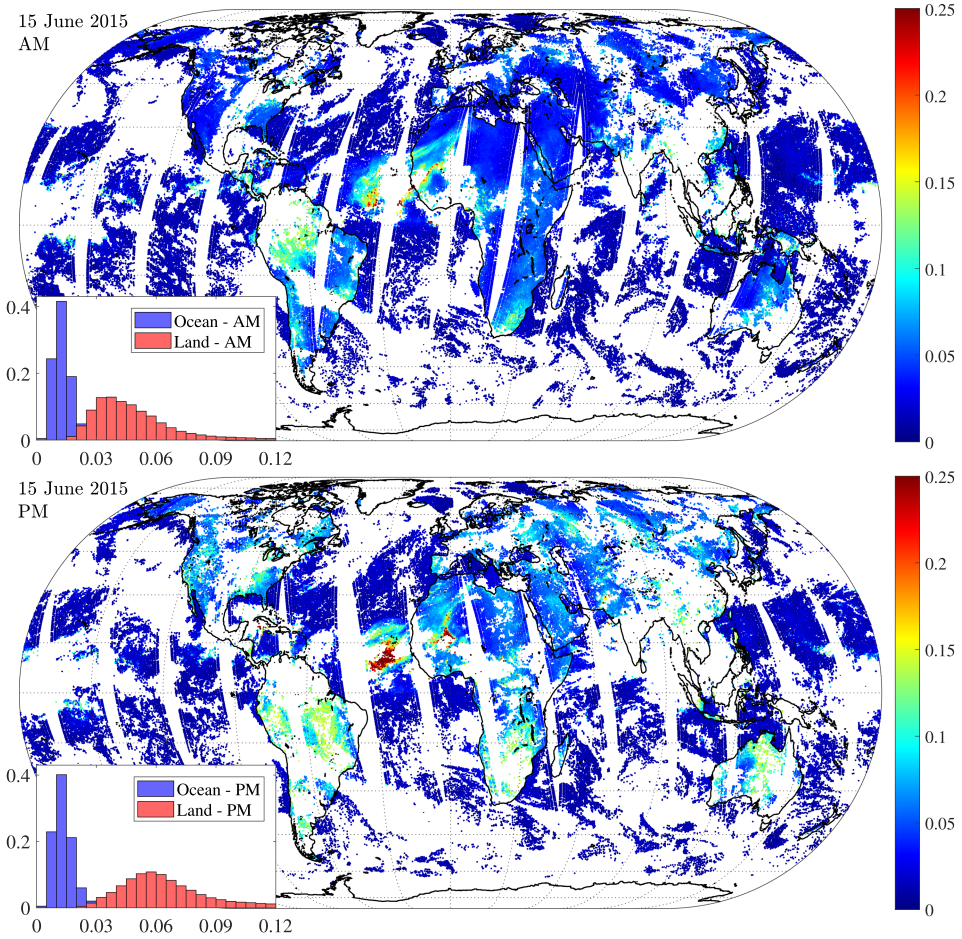

Figure 8. IASI-retrieved absolute OD uncertainties for 15 June 2015 for the morning (top) and evening (bottom) overpass. The insets provide the probability histograms of the global data. IASI = Infrared Atmospheric Sounding Interferometer; OD = optical depth.

North Africa, parts of Europe, and central and south Asia, and over ocean: the North Atlantic Ocean, the Caribbean Sea, the Mediterranean Sea, the Red Sea, the Arabian Sea, and Indian Ocean. Especially noticeable is the large dust plume over north West Africa and the North Atlantic Ocean, which is fairly consistent across land-ocean and morning-evening overpass. Over remote regions, the OD values are close to and centered around 0 but are noticeably less noisy over ocean than over land, a direct consequence of the fact that detection is easier over ocean due to the more uniform surface emissivity. Certain land areas also exhibit small local biases (e.g., southeastern part of Africa) .

4.3. Uncertainty Estimates and Postfiltering

The calculation of the uncertainty follows closely Whitburn et al. (2016), and is calculated by propagation of the uncertainty of the different input parameters of the NN, augmented with a (conservative) 10% uncertainty to take into account errors in the NN. The total uncertainty is estimated in absolute terms and is always positive, being obtained from the sum of the squares of the different contributions. Over land, the uncertainty due to R dominates heavily, especially during nighttime, where the thermal contrast is low. The other important uncertainty stems from the altitude/temperature of the layer; this is generally the most important term over oceans. For a given state of the atmosphere and the surface (i.e., for a given CR generated by the NN) the contribution of the uncertainty due to R to the total uncertainty decreases with increasing dust loadings, and for high loadings of dust an almost constant relative uncertainty is obtained. The estimated total uncertainties for 15 June 2015 are shown in Figure 8, both as a global distribution and as histogram. In the presence of detectable dust, uncertainties are of the order of 15–30%. Elsewhere, the majority of the uncertainties are in absolute value in the 0.01–0.02 range over ocean and 0.04–0.06 over land. The uncertainties over land during the morning overpass are noticeably smaller due to the better thermal contrast. Finally,

note that over some land areas (e.g., South America), some scan angle dependence could be observed for DODs close to 0. The reason for this is not clear and it is also not easily corrected for, as it seems present in the dust index itself. Fortunately, such a dependence is not seen in the areas most affected by dust.

At the end of the retrieval, the measurements are postprocessed to remove any clear erroneous retrievals or retrievals for which the measurement carries no meaningful information. A first criterion removes large negative retrievals, below an DOD of −0.1 or with an R value below −3. These are obvious candidates as their large unphysical value goes beyond the expected random noise. Next, all retrievals are removed for which the CR exceeds 0.15, corresponding to conditions where the measurement sensitivity is extremely low. Finally, the observations are also flagged if both the absolute and relative uncertainty simultaneously exceed a threshold of 0.15 and 50%, respectively. The criterion on the absolute uncertainty is mostly relevant for observations with little or no detectable dust, while the criterion on the relative uncertainty is meaningful for observations with a detectable dust signature. As a whole, this postfiltering procedure keeps about 98–99% of the ocean measurements and about 60–97% of the land data (worst in the winter nighttime overpass, best in the summer daytime overpass).

4.4. DOD at 550 nm

AODs are most often reported at 550 nm as most satellite remote measurements and ground-based measurement operate in the visible. Consequently, it is also the quantity that is most optimized in dust models. For these reasons, it is convenient to convert our retrieved DOD at 10 μm to a DOD at 550 nm. The conversion is unfortunately not straightforward and depends on the specific particle size distribution and spectral variations in the refractive index data. Highwood et al. (2003) report ratios DOD550:DOD10 between 1.68 and 2.91 for three different dust models. A similar range was found (Pierangelo et al., 2004) from theoretical calculations using retrieved AERONET size distributions at Capo Verde (1.8–2.5). Considering only coarse mode particles, Capelle et al., (2014, 2018) and Cuesta et al. (2015) calculated conversion factors in the range of 0.9–2.5. Empirical conversion factors between IASI and total visible AOD from a series of satellite instruments were found to be in the range 1.5–3.5 (Peyridieu et al., 2013). Here we use a constant conversion factor of 2 to obtain an approximate DOD at 550 nm, bearing in mind that large regional or even episodic biases can be expected (the reader is referred to (Capelle et al., 2014, 2018; Peyridieu et al., 2013) for insightful discussions on this topic).

5. Evaluation and Comparison

5.1. Comparisons With AERONET

AERONET (https://aeronet.gsfc.nasa.gov/; Holben et al., 2001) is a large network of ground-based Sun photometers dedicated to measuring AOD and a variety of other aerosol parameters. The network offers accurate standardized measurements over a long time frame and in many locations in the world. AERONET is the preferred choice for validating aerosol models and satellite measurements of aerosols (e.g., Popp et al., 2016; Sayer et al., 2013). A preliminary comparison of an earlier version of the current product (v5) and of several other IASI dust products with AERONET data over a restricted region was already reported in Popp et al. (2016). Validation of IASI dust products with AERONET have also been presented in Cuesta et al. (2015) and Capelle et al., (2014, 2018). Here we follow largely the comparison methodology detailed in those papers. In particular, the retrieved DOD at 550 nm is compared with the coarse mode AERONET product as produced by the Spectral Deconvolution Algorithm (SDA v4.1 of AERONET V3, Level 2.0) (O'Neill et al., 2003). The motivation is twofold: (i) the coarse mode AOD is a good approximation for the coarse mode DOD in the areas that are dominated by dust (over oceans and in coastal regions, sea salt can account for an offset of about 0.05–0.1; see, e.g., Spada et al., 2013) and (ii) fine nondust aerosols, which dominate in large parts of the world the AERONET total AOD, are completely removed. Note that by limiting ourselves to the coarse mode, we neglect the contribution of the fine mode to the DOD. This contribution is however relatively small (typically 20–30% of the total AOD in the AERONET SDA product over sites dominated by dust) and importantly, neglecting this term actually helps the comparison since the retrieved DOD in the infrared is largely insensitive to variations in the fine mode. The SDA coarse mode AOD are given at 500 nm; for the comparison we converted these into a coarse mode AOD at 550 nm using equation (1) of O'Neill et al. (2003).

We followed the usual approach of comparing the AERONET data with the satellite data on an overpass basis (Capelle et al., 2018; Sayer et al., 2013); that is, AERONET data are averaged in a time window of ±30 min of the IASI overpass time and compared with IASI data averaged within a distance of 30 km of the AERONET site. The alternative of comparing individual IASI measurements within 30 km with the closest match in

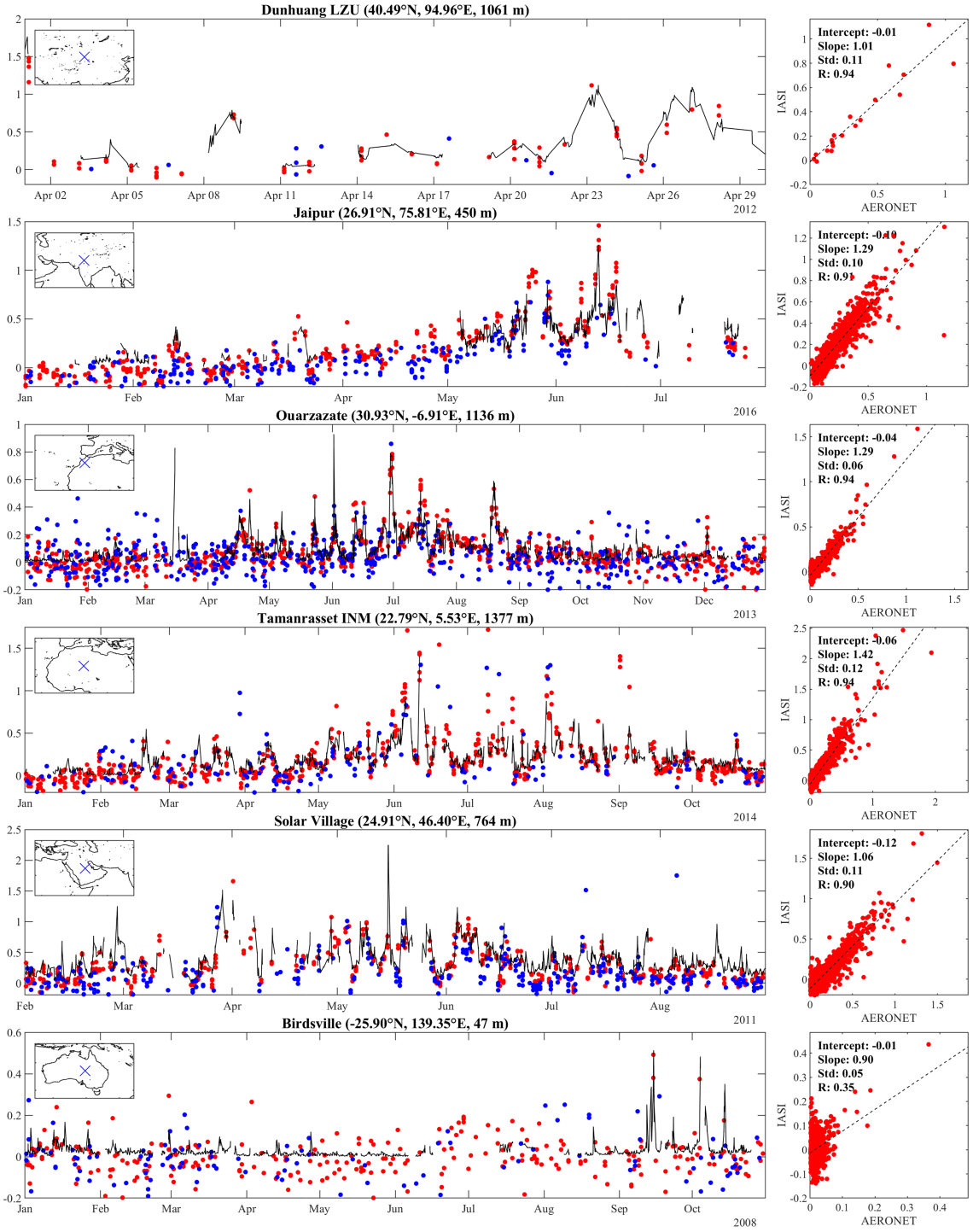

Figure 9. AERONET AOD coarse mode at 550 nm versus IASI DOD at 550 nm for selected sites near or in source regions. Time series on the left show all available individual AERONET measurements for a selected time period (black line) and the individual IASI measurements within 30 km of the site (red, morning overpass; blue, evening overpass). The scatter plots on the right show all the available overpass-averaged data pairs for each station for the entire 10 years 2008–2017. AERONET = AErosol RObotic NETwork; AOD = aerosol optical depth; IASI = Infrared Atmospheric Sounding Interferometer; DOD = dust optical depth.

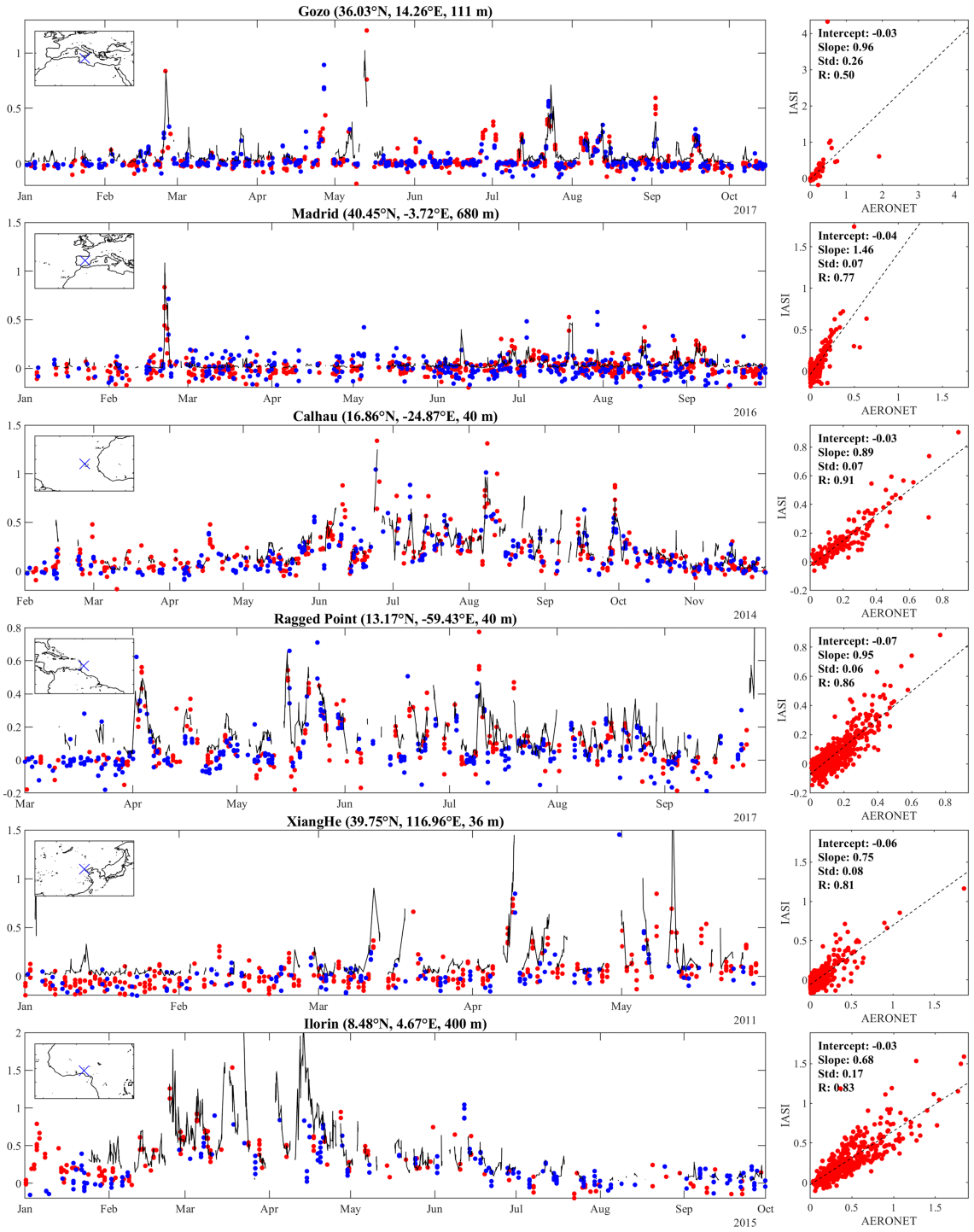

Figure 10. Same as Figure 9 but for stations located further from the source regions.

time provides an increased number of comparison pairs but with a larger scatter. We used all valid IASI retrievals, even those with a high uncertainty but removed uncertain AERONET measurements using the criterion derived in Capelle et al. (2018). However, unlike in that paper, we do not exclude IASI-AERONET pairs with a difference in OD larger than some predefined threshold (the so-called outliers).

Examples are presented in Figures 9 and 10 for selected sites. All collocated overpass-averaged pairs between 2008 and 2017 are shown in scatter plots on the right, together with some statistics (intercept and slope of

the regression line, standard deviation of the differences, and the correlation coefficient). The time series on the left show all individual measurements available from each AERONET station (black line) over a selected time period and the IASI measurements over each station within 30 km (data from the morning overpass is displayed in red, evening overpass in blue). In contrast to the scatter plots on the right, no data are averaged in these time series plots, and also data which is not collocated in time is shown.

Figure 9 shows the results of stations located in or near large deserts: Dunhuang LZU (Gobi desert and downwind the Taklimakan and Kumtag desert; Bi et al., 2014), Jaipur (India, close to the Thar desert; Verma et al., 2013), Ouarzazate (Morocco, northwest of Sahara desert), Tamanrasset (Saharan desert; Guirado et al., 2014), Solar Village (Arabian desert, Saudi Arabia) and Birdsville (Australia, between the Simpson desert and the Strzelecki desert; Mitchell et al., 2017). From the time series plots it is immediately clear that IASI is not only capable of capturing the large seasonal trends of dust over deserts but also the day-to-day variability. This is also obvious from the scatter plots with correlation coefficients above 0.9, demonstrating a very close correlation between the two data sets. Occasionally (e.g., over Ouarzazate and Tamanrasset), there is no matching IASI data for strong dust events captured by AERONET and vice versa. Differences in cloud screening between the two data sets seem to be at the origin. The center of large dust plumes in particular are sometimes erroneously marked as cloudy in the IASI L2 data. Regression slopes vary between 1.06 and 1.42 for the selected sites, indicating that for the emission regions, the infrared to visible conversion factor of 2 is slightly too large. The offsets from the regression fits range from −0.01 to −0.12, pointing to either a low bias in the IASI data (due to, e.g., emissivity effects, reduced sensitivity to dust in the boundary layer, or biases in the dust index), or a high bias in the AERONET data (due to, e.g., contributions of aerosol other than dust). Observe that despite the reduced sensitivity in the evening, there is an agreement between the morning overpass data (red) and the evening overpass data (blue). This is expected given that dust events are episodic and characterized by variability that generally takes places over timescales longer than 1 day (Ridley et al., 2012; Smirnov et al., 2002; Wang et al., 2004). A small but systematic morning-evening offset is apparent at some sites in the IASI data (around 0.05 at Jaipur and Solar Village), and likely linked to the reduced sensitivity in the evening. Birdsville, which we excluded from the above discussion, is illustrative for sites with very low average OD. Apart from a few sporadic dust events, which are nicely captured by IASI, Birdsville has a mean AERONET AOD of just 0.02 ± 0.01. With an IASI DOD average of 0.00 ± 0.05, the satellite retrievals are about as good as could be hoped for over this desert site, even with a correlation coefficient of 0.35.

Examples of stations located near oceans and located further from source regions are given in Figure 10; they are as follows: Gozo (Malta, Mediterranean Sea), Madrid (Spain), Calhau (Sao Vicente, Cape Verde, west African coast; Gehlot et al., 2015), Ragged Point (Barbados; Prospero & Mayol-Bracero, 2013), XiangHe (North China Plain; Xia et al., 2013), and Illorin (Nigaria, sub-Sahel; Pinker et al., 2010). Compared to the emission regions, the correlation coefficients are naturally a little lower as several of these sites only have intermittent dust episodes. However, overall the data sets correlate again very well, and what was said above with respect to intercept applies here as well. The agreement between day and night is even closer than for the emission regions, in line with what can be expected. The comparisons over stations in the Atlantic and in the North China Plain demonstrate the capability of the algorithm to measure accurately DOD from dust transported over small and large distances. The performance for stations near the ocean (Calhau, Gozo) benefits in addition from the reduced retrieval noise over oceans. In terms of regression slopes, two stations stand out. The lower regression slope for Illorin likely relates to an almost year-round low thermal contrast in that part of the world. This leads to a reduced sensitivity of the IASI measurement to the lowest atmospheric layers and that might cause the retrieval to miss all or part of the dust column. Madrid has with 1.46 a rather large regression slope for unclear reasons (see below).

It is instructive to discuss the two outliers seen in the correlation plot of Gozo. An IASI DOD of 4.3 and corresponding AERONET value of 0.48 was observed on 15 May 2015. Dust is generally transported over the Mediterranean in a more or less direct way by southerly winds (Mona et al., 2006). However, the dust plume that was observed on the 15th underwent a long trajectory before arriving to Gozo. It can be traced back to 10 May 2015, where it was observed off the west coast of Africa and the Atlantic, after which it moved northward, over the south of Spain, and made its way slowly into the Mediterranean basin. The atypical transport took place at a much higher altitude (up to 10 km judging from the Cloud-Aerosol Lidar and Infrared Pathfinder Satellite Observation transect over the Mediterranean on the 14th) than the usual direct routes. This example illustrates well that inappropriate climatological height input can lead to large errors

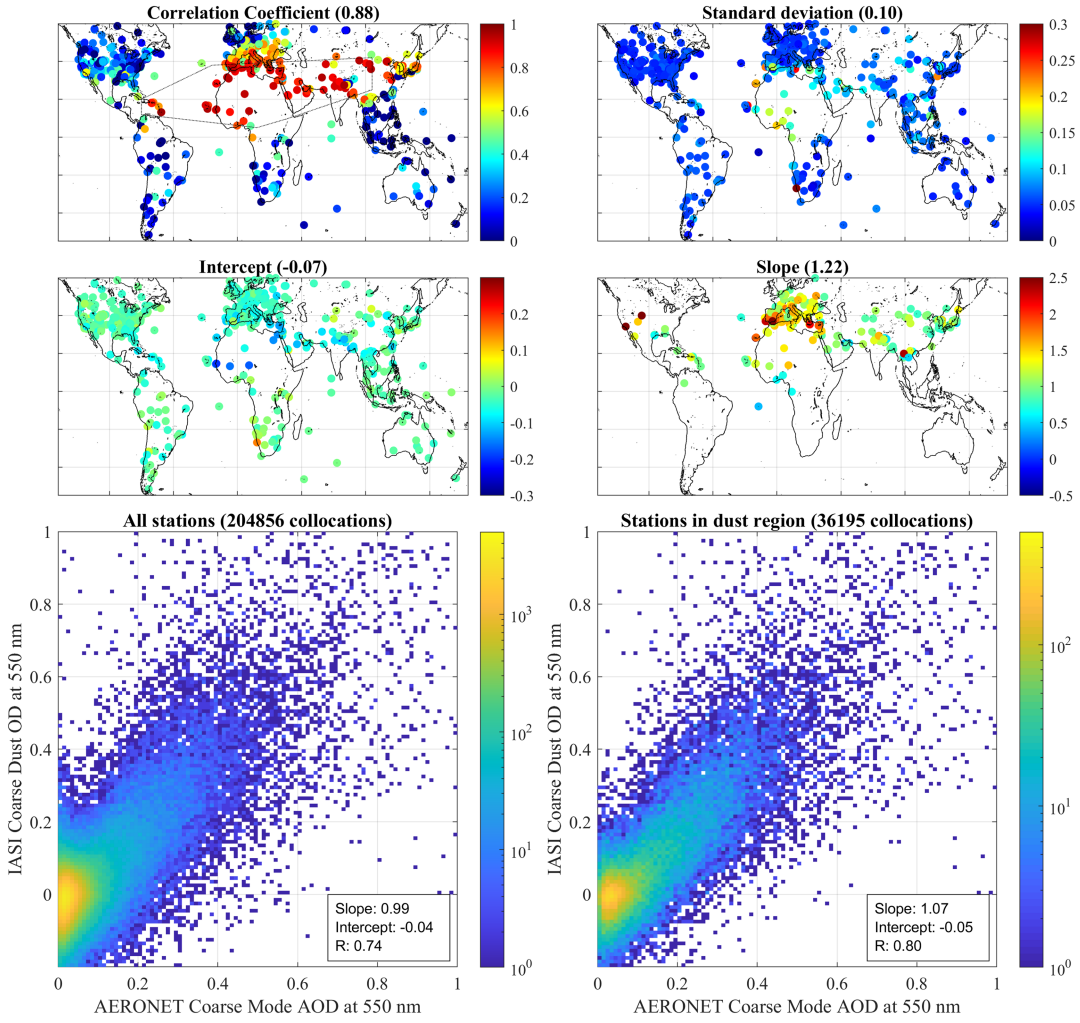

Figure 11. Global regression statistics of the AERONET AOD coarse mode at 550 nm versus IASI DOD at 550 nm comparison for all AERONET sites. The numbers between brackets in the first four subplots are median values of the individual regression coefficients for all stations located in the dust region. This region is shown in the first subplot. The bottom plots are bivariate histograms on a log scale of all matched data (left) and in the dust zone (right). AERONET = AErosol RObotic NETwork; AOD = aerosol optical depth; IASI = Infrared Atmospheric Sounding Interferometer; DOD = dust optical depth.

in the retrieval. In such cases, a dedicated dust altitude retrieval or daily modeled altitude forecasts would be beneficial. The other outlier over Gozo corresponds to an observation made on 11 May 2016. This observation, and several other nearby observations, have an elevated inversion index R_{inv} (see section 2.4) indicating the presence of a large negative temperature difference between water and the atmosphere directly above it. However, whereas most of these were removed prior to the dust retrieval as part of the prefilter, the observation above Gozo managed to pass this filter. As the retrieval does not account for the inversion effect, an underestimated OD is retrieved. It should be stressed that these two observations are atypical and that for the other 214 collocations a much better agreement is seen. By excluding these two outliers from the statistics the correlation coefficient over Gozo increases from 0.5 to 0.88. Such outliers also explain the lower correlation coefficients over a few other sites in the larger dust region defined below.

A statistical summary of the comparison is presented in Figure 11 for all AERONET sites with at least 10 collocated IASI measurements. Shown are the correlation coefficients and standard deviations (top), regression intercepts and regression slopes for sites with a correlation coefficient over 0.5 (middle panels), and bivariate histograms of all matched pairs for all stations (left bottom) and for all stations in a large zone around Sahara and Asian deserts (right bottom). This zone is defined in the top left panel and for convenience will be referred to as the "dust region." Inside the dust region, the median correlation coefficient

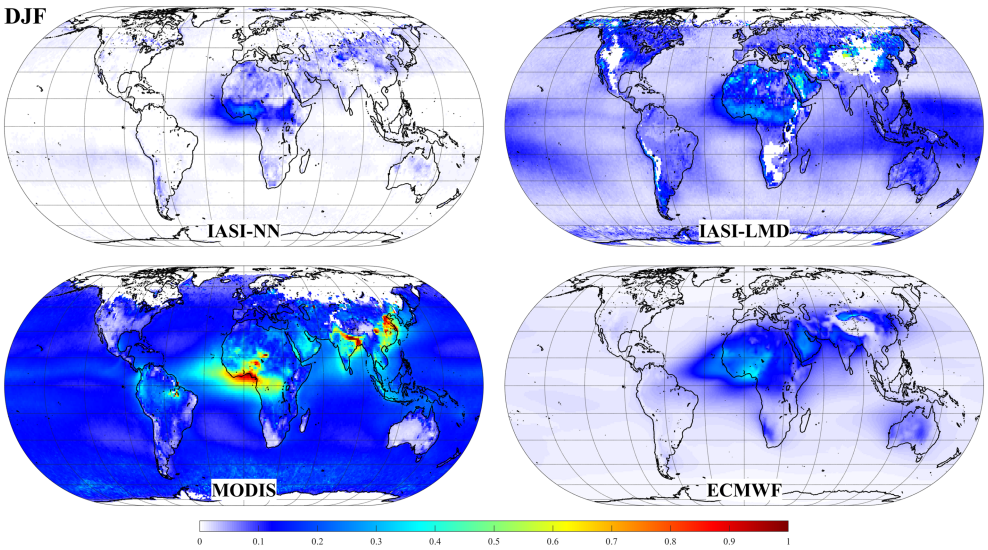

Figure 12. The 2008–2017 December-January-February climatology of the DOD at 550 nm of the IASI-NN product (top left), IASI-LMD product (top right), the total AOD at 550 nm of MODIS (bottom left), and the ECMWF model (bottom right). DOD = dust optical depth; IASI = Infrared Atmospheric Sounding Interferometer; AOD = aerosol optical depth; MODIS = Moderate Resolution Imaging Spectroradiometer; ECMWF = European Centre for Medium-Range Weather Forecasts.

is 0.88 confirming the remarkable correlation between the two data sets on a site basis. Outside, the lower correlation coefficients are a result of the absence of dust rather than the lack of retrieval skill as explained with the example of Birdsville above. In fact, the very low correlations over areas where no dust is expected (e.g., Maritime Southeast Asia), demonstrate the robustness of the retrieval product against other types of coarse aerosols (e.g., sea spray). The median standard deviation for stations in the dust region is 0.1 and 0.06 outside, in line with the retrieval uncertainty estimate of the DOD at 10 μm of 0.05 over land (see section 4.3). The regression intercepts are, as previously noted, slightly negative (−0.07) over the dust region. The biases are largest just south of the Sahel (e.g., −0.17 for Zinder Airport in Southern Niger) and likely linked to residual biases of the dust index related to surface emissivity. For the rest of the world, the regression intercepts are smaller (median of −0.025).

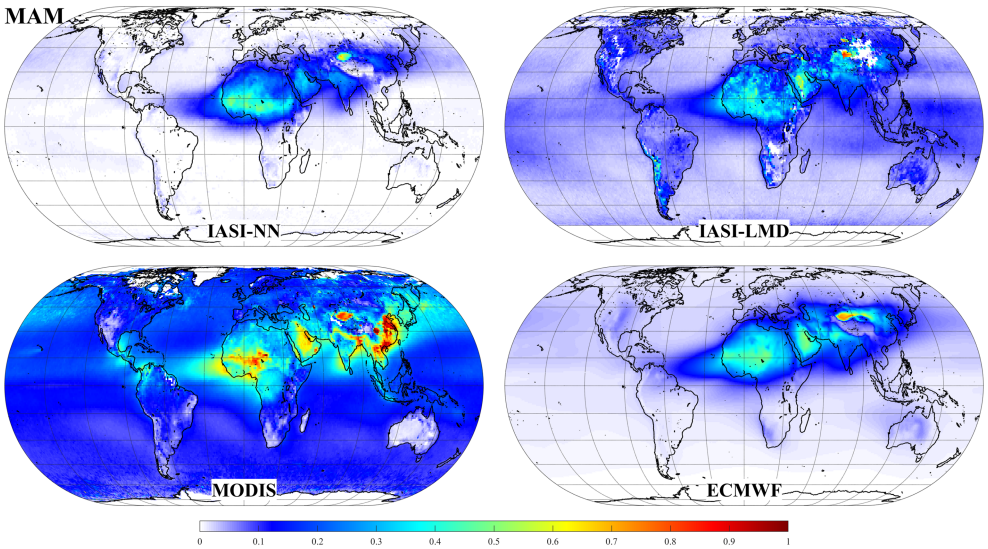

Figure 13. Same as Figure 12 for March, April, and May.

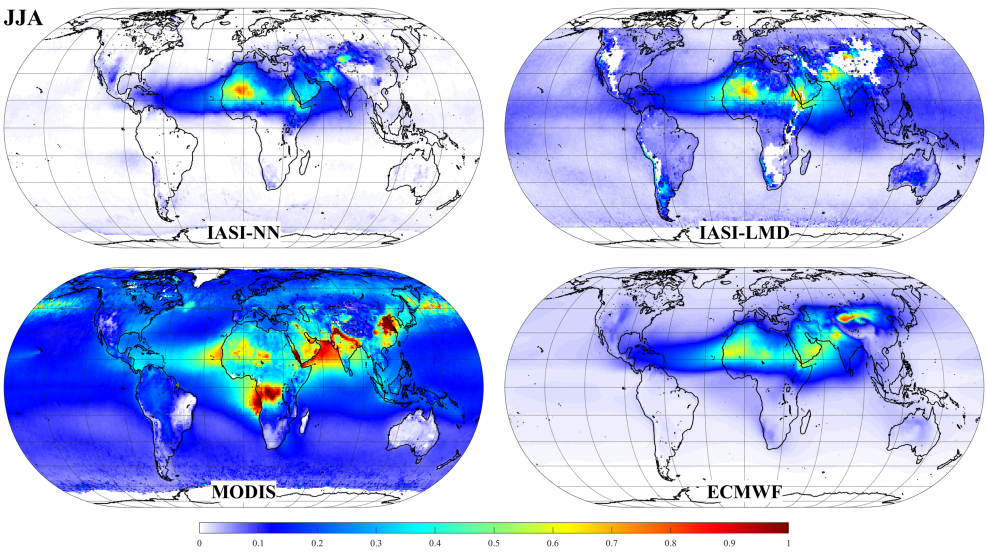

Figure 14. Same as Figure 12 for June, July, and August.

The summary plot of the regression slopes confirms with a median value of 1.22 that the infrared-to-visible conversion factor of 2 is on average slightly too large. The stations in Africa north of 10°N stand out with a median slope of 1.42, compared to slopes of around 1 for stations in Asia. These biases could relate to the fact that the dust Jacobian, which is used in the calculation of the dust index (see section 2), was built from spectra observed over Morocco. However, it seems unlikely that this also explains why many stations in south Europe have much higher slopes than in the rest of the world (over 2), as illustrated before with the example of Madrid. These possibly relate to biases in the dust height climatology, dependences of the infrared-to-visible conversion factor on size distribution and composition, and assumptions in the AERONET SDA retrieval algorithm. The lower slope seen at Ilorin is also seen at other stations of West Africa around the gulf of Guinea. While for a variety of reasons, the slopes differ from site to site, the fact that very high correlation coefficients are reached implies that for a given site the true conversion factor does not vary significantly throughout the year or from year to year. The IASI data set can therefore reliably be used to reveal the temporal variability of DOD at 550 nm at a given location.

The bivariate histograms in Figure 11 summarize the performance when all matched pairs are grouped. The reported regression statistics are in line with what is reported above for the individual sites. The advantage

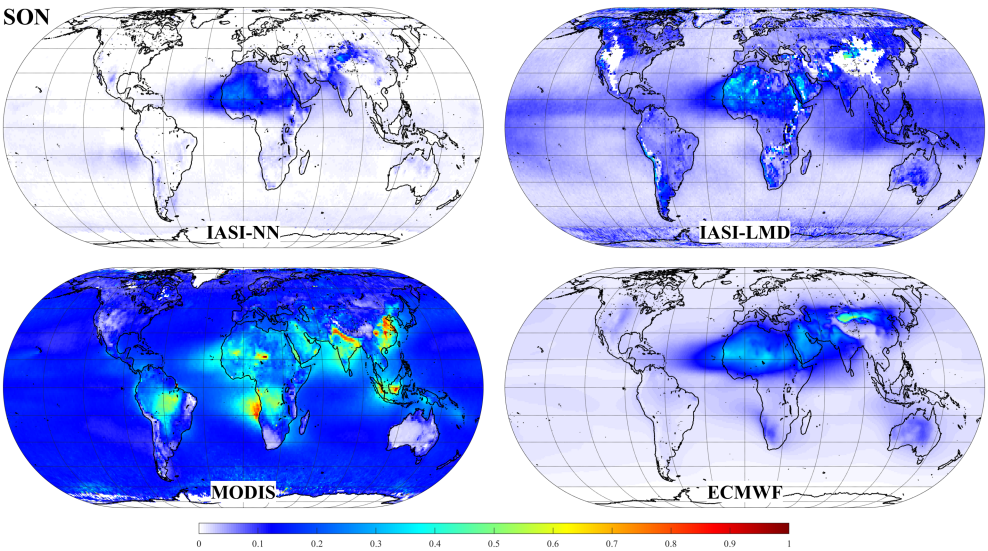

Figure 15. Same as Figure 12 for September, October, and November.

of allowing negative retrievals in the algorithm is particularly obvious from these plots: It allows an (almost) unbiased product, with a mean of AOD of −0.01 for IASI retrievals corresponding to an AERONET AOD below 0.05. The average negative intercepts of −0.05/−0.04 are likely due to contributions of nondust aerosol to AERONET AOD which averages around 0.01–0.06 outside the dust region.

5.2. L3 Data, Seasonal Climatology, and Comparison With Other Products

End users most often chose to work with gridded averaged data (called L3 data), as these are easier to handle, analyze, and visualize than the L2, thanks to their smaller (file) size and regular spatial grid. Averaged data also has a reduced random noise, and this helps in revealing spatial and temporal patterns. However, the process of averaging can introduce or amplify errors in the data set. In particular, sampling biases in the original data can propagate to data biases in averaged data. For instance in our case, as the retrieval systematically removes scenes with large temperature inversions over oceans, a monthly average will necessarily be biased toward scenes with specific meteorological conditions (temperatures or wind patterns). These can be correlated with the presence or absence of dust, causing a biased average. Variable measurement accuracy is another factor which can introduce biases. The presence of false outliers in particular can vastly skew an average. For these reasons, whenever possible, and especially for validation, it is always better to use raw L2 data. We refer the reader to Levy et al. (2009), Schutgens et al. (2017), and Sun et al. (2018) for a discussion of these issues and for an overview of different averaging approaches.

That being said, a L3 data set has been created alongside the L2 described in this paper. Daily and monthly $1° \times 1°$ grids were produced by the simplest and most common approach of binned averaging. This approach consists of assigning to each grid box the arithmetic mean of all retrieved measurements whose footprint center is located in the grid box under consideration. The introduction of negative values in the retrieval, as explained before, is required for obtaining an overall unbiased product. However, after averaging 1 month of data, these negative values have fulfilled their purpose. Negative monthly average grid cells are therefore set to 0 in the L3 data to provide a better estimate of the true monthly average.

We now have a closer look at the seasonal climatological averages of the IASI DOD at 550 nm, obtained from averaging 10 years of monthly L3 data. They are presented in Figures 12–15, along with climatologies of other related products:

- The third-party IASI-derived monthly DOD product, produced by the LMD group. This product is based on LUTs and has a long and active development history, see Capelle et al. (2018), Pierangelo et al. (2004), and references therein. The most recent version (2.2) of the publicly available monthly gridded L3 data was used here.
- A MODIS climatology of total AOD, derived from the officially distributed monthly MOD08_M3 v6.1, combined Dark Target and Deep Blue data set (Levy et al., 2013; Platnick, 2017; Sayer et al., 2014). Important differences between MODIS and the other products are expected, as the MODIS AOD includes the contribution of other aerosols, in particular from smoke (Africa, South America), anthropogenic pollution (Asia), and sea salt aerosols over the oceans.
- ECMWF modeled DOD: MACC reanalysis (Inness et al., 2013) for the period 2008–2012 and CAMS near-real-time data set (Flemming et al., 2017) for 2013–2017. While no full consistent data set is available, both runs depend on the same aerosol module (Morcrette et al., 2009) and assimilation of MODIS data.

Some general observations can be made from comparing the four distributions. First, a qualitative agreement between the IASI-NN product and the ECMWF dust model can be observed over the entire globe, in terms of enhancements over source areas, main transport patterns, and performance over remote areas. This demonstrates the capability of the IASI-NN algorithm to single out dust aerosol from other aerosol on a global scale, its sensitivity to even weak dust loadings, and its robustness against surface emissivity effects. Comparison with the total AOD MODIS product makes the advantages of a dedicated DOD product apparent, for example, for improving dust models. In terms of background OD over remote areas, the NN retrieval averages out close to the expected zero value for all seasons. Very slight positive biases appear in the South Pacific off the west coast of South America and in the Southern Ocean due to cloud contamination (see next section). Whereas in the MODIS total AOD a larger background value is expected due to the contribution of other aerosols, regional biases of the order of 0.1–0.2 are observed over both ocean and land in the LMD product. Another difference with the LMD product is that the NN product is notably smoother over deserts, likely due to a better treatment of surface emissivity. For instance, the Arabian-Nubian Shield (outcrop located along both sides of the Red Sea) is apparent in all seasons in the LMD product (compare also with

Figure 2). Despite the difficulty of retrieving dust over desert surfaces in the infrared, both IASI products demonstrate in the mean a very good consistency across land-ocean transitions, especially when compared with the MODIS merged product, where dust over oceans seems to be overestimated relative to land.

Let us now take a closer look at each season separately. The information on global dust sources was primarily obtained from Ginoux et al. (2012), Varga (2012), and Varga and Szalai (2013).

Winter (December-January-February). The main global source of atmospheric dust in the winter months is Bodélé depression, northeast of Lake Chad (Washington et al., 2009). Northeastern trade winds (the Harmattan) in winter and early spring transport the dust over West Africa and over the Gulf of Guinea (Cuevas et al., 2015; Ridley et al., 2012). This main transport pathway is well seen in all four products. The Bodélé depression itself is readily seen in the MODIS data but only barely noticeable in the IASI-NN data (in the LMD data it is not seen at all). This is likely the result of the low mean dust altitude over the depression (see Figure 6), which reduces the measurement sensitivity. The winter is also the season with frequent fires in the sub-Sahel region between 5°N and 15°N (Giglio et al., 2006). These contribute to the much higher AOD observed from MODIS over central Africa and its west coast. Dust is identifiable from the model output in the winter directly over the Saharan desert, the Arabian desert, and the Taklamakan desert. This is not really seen in the IASI data. Over the Saharan desert and the Sahel, this could be related to the low mean dust altitude in the winter (see Figure 6). With hardly any dust detected over the deserts in the Southern Hemisphere, MODIS and IASI-NN provide a consistent picture, whereas the model seems to overestimate the OD over the Namib and Australian deserts.

Spring (March-April-May). As in winter, most dust in Africa originates from the southern part of the Saharan desert and the Sahel region (Mauritania, Mali, Niger, and Chad). The more easterly trade winds are seen here to carry the dust 5,000 km across the Atlantic toward Venezuela. The four products also exhibit good similarity in the OD enhancements observed over the central part of the Arabian desert. Another source region is the Indo Gagentic plain, with a hot spot over the Thar desert and transport over the rest of India and Indian Ocean, seen in both IASI data sets and the model. Surprisingly, the Thar desert constitutes a local dip in the MODIS AOD. This is seen in all seasons at exactly the same place, indicative of a surface related retrieval artifact. Spring is the season with most airborne dust in East Asia (e.g., Chen et al., 2017 and references therein), mainly originating from the Tarim basin/Taklamakan desert and high-altitude eastward transport over the Pacific toward the United States and Canada. A remarkable good agreement is seen between IASI-NN and the model, especially with respect to the transport over ocean. Observe in particular the small increase in background concentrations over the North Atlantic Ocean (between 30°N and 60°N) in the IASI-NN product. This is not observed in the other seasons and demonstrates again how well IASI is able to discriminate dust. While the LMD retrieval captures the main long-range transport pattern over ocean, its performance over East Asia is less good (partially noisy and partially absent retrievals over high-altitude areas).

Summer (June-July-August). The North African dust belt moves up further north in summer. The Taoudeni Basin/El Djouf desert in Mali and Mauritania appears to be the main source area in the Saharan desert. Globally, DOD over 0.5 are also observed in the IASI data over the Tokar delta in northeast Sudan, the Arabian desert, and Taklamakan desert. A very good qualitative agreement is reached between the two IASI products (this work and the LMD product) and the model over these principal source areas. However, in the IASI-NN data there is a notable relative underestimation of the Asian compared to the African sources (or an overestimation of the latter). This feature has been pointed out also in the discussion of the regression slope (Figure 11) in the comparison with AERONET and, as said then, is likely due to the preferential sensitivity of the dust index to specific mineralogies. Compared with MODIS, IASI is relatively insensitive directly above some dust sources (Bodélé depression, Iran, and Oman). Finally, note that in this season a large hot spot is seen over central Africa in the MODIS data due to smoke from the yearly recurring fires in this region. As with (other) anthropogenic aerosols, these are neither seen in the IASI data nor in the model as these represent the optical depth due to dust only.

Autumn (September-October-November). Autumn resembles summer in terms of source areas and transport patterns but with much lower average quantities of dust. On a global scale, the agreement between IASI-NN data and the model is also good in this season.

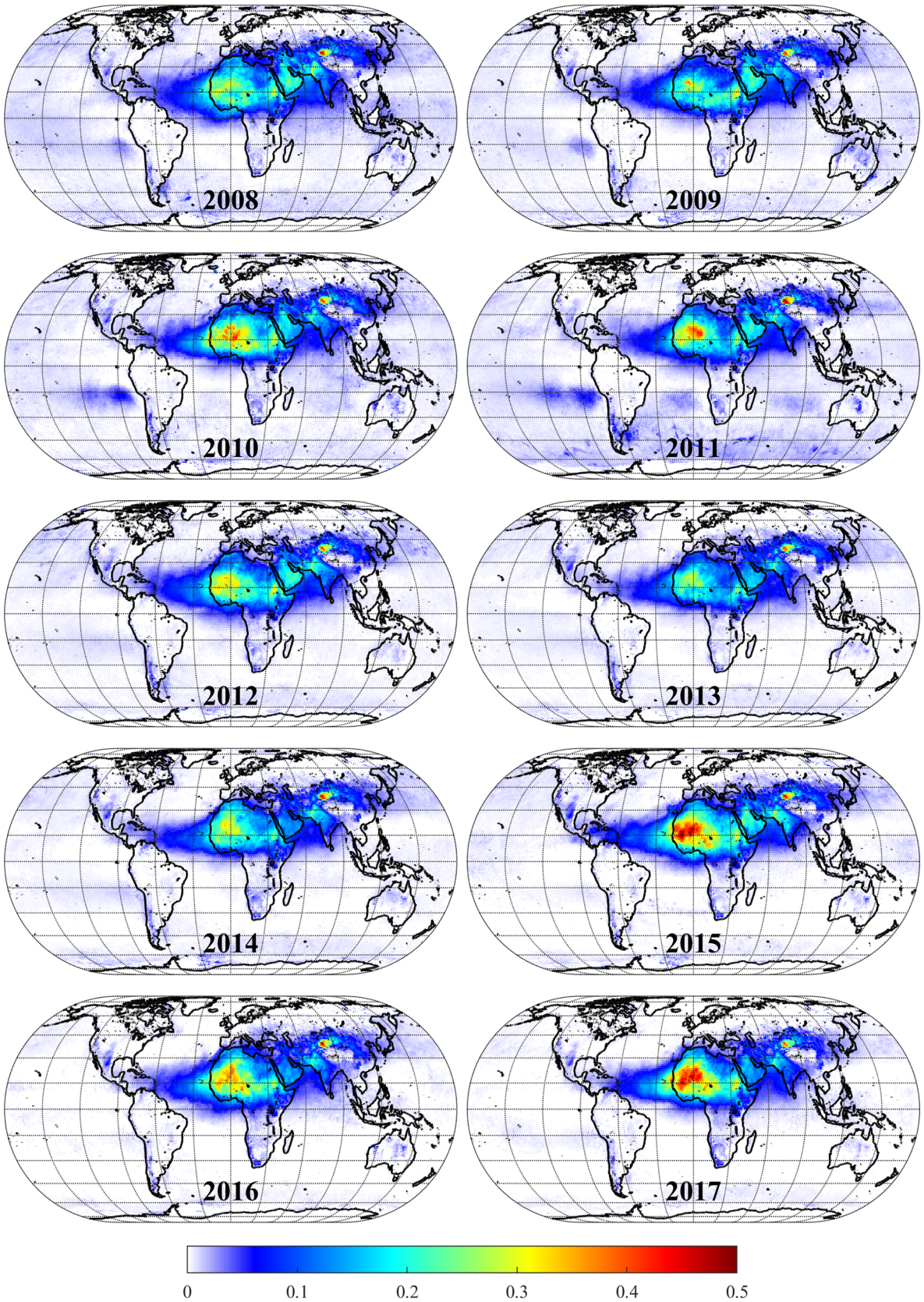

Figure 16. IASI-derived yearly averaged dust optical depth at 550 nm for the period 2008–2017. IASI = Infrared Atmospheric Sounding Interferometer.

6. Conclusion

In this paper, we have presented a new algorithm for retrieving infrared DOD from IASI satellite observations. It is based on the calculation of a pseudoquantitative dust index and subsequent conversion to the 10-μm OD through an artificial NN. Compared to other more physically based algorithms, the current retrieval does not attempt to reconstruct the observed spectrum; instead, the NN serves as an explicit statistical inverse model. Some of the advantages of the present algorithm are an inherent good sensitivity to dust, the ability to discriminate dust aerosol from other aerosols and molecular absorptions that affect the baseline of the spectrum, its good performance over land thanks to the possibility of a straightforward correction of surface emissivity artifacts, and its theoretical unbiasedness.

Relying on a constant conversion factor, the DOD at 10 μm can be converted into an approximate DOD at 550 nm, which allows comparison with independent measurement performed in the visible. The comparison with coarse mode AERONET data demonstrates that the IASI-retrieved DOD at 550 nm is on an absolute level in good agreement with the AERONET data over sites where dust is the dominant aerosol type. On a relative basis, the agreement is even better (with a median correlation coefficient of 0.88), implying that for a given location the IASI data set can be used to accurately track in time relative changes in the DOD. This opens perspectives of exploitation of the IASI data set by dust models and its use for dust forecasting. In addition to the availability of the measurements during both day and night, the capability of IASI to accurately single out dust from other aerosols is an important advantage compared to sounders operating in the visible. For best results, assimilation approaches will need to be adapted to constrain the model in a local relative way.

Future product developments will be directed toward improving some of the limitations and weaknesses of the current algorithm. In particular, this includes (1) the retrieval of altitude information to complement the dust altitude climatology, (2) the retrieval over scenes with large temperature inversions, and (3) solving the current observed biases between African and Asian dust sources. In addition, the use of more spectral channels could be envisaged to increase further the sensitivity of the retrieval.

Over 10 years of IASI-A data are now publicly available (see the section on data availability below). Figure 16 shows the yearly averaged DOD at 550 nm aggregated from the monthly L3 data for the 10 years of available data. The large year-to-year variability is notable. Dust events correlate with local meteorology and large scale climatological phenomena such as the El Niño–Southern Oscillation (Evan et al., 2016; Xi & Sokolik, 2015, and references therein). While an analysis study of these in the context of the present data set is out of the scope of the present study, it is clear that the IASI decadal data set of global and bidaily atmospheric dust constitutes a unique record that can be used to explore driving factors of emission, transport, and deposition. One caveat though, is that the data set is based on the operationally distributed IASI L2 meteorological data. The underlying algorithms have undergone several updates over time (see in this context also Van Damme et al., 2017). For instance, important improvements were introduced to the official IASI cloud detection algorithm in 2011–2012, as is apparent from the noticeably reduced cloud contamination in 2012 (see Figure 16). Back processing of the IASI L2 is foreseen in the near future, at which point also the dust data set will be reprocessed to build a completely homogeneous record. Currently IASI-A is slowly nearing decommissioning; however, with the 2012 launch of IASI-B, and the planned launch of IASI-C end of 2018, the IASI data set is expected to cover eventually over 20 years of data. After that, a new generation of improved IASI instruments is planned (also three instruments, currently foreseen to be launched from 2022; Crevoisier et al., 2014), guaranteeing the long-term future of hyperspectral infrared remote sensing and of infrared measurements of atmospheric dust in particular.

Data Availability

The 2008–2017 data (L2 and 1° × 1° daily and monthly L3) presented in this study are available from the ICARE Data and Services Center http://www.icare.univ-lille1.fr/ and within the framework Copernicus Climate Change Service (C3S). This data set will be expanded up until at least 2020. In the future, the product described in this paper will also be operationally distributed by EUMETCast, under the auspices of the Eumetsat Atmospheric Monitoring Satellite Application Facility (AC-SAF; http://ac-saf.eumetsat.int). The CALIPSO dust altitude climatology presented in this work is available from the corresponding author upon request.

Acknowledgments
This work was supported by the European Space Agency (ESA) as part of the Aerosol-CCI project and by the Copernicus Climate Change Service (C3S). L. C. is a research associate supported by the Belgian F.R.S.-FNRS. The research was also funded by the Belgian State Federal Office for Scientific, Technical and Cultural Affairs (Prodex arrangement IASI.FLOW). IASI is a joint mission of EUMETSAT and the Centre National d'Études spatiales (CNES, France). It is flown on board the Metop satellites as part of the EUMETSAT Polar System. The IASI L1c and L2 data are received through the EUMETCast near-real-time data distribution service. We thank T. August and T. Hultberg for providing an early copy of the IASI L2 version 6 data for the year 2013, D. Zhou for making the land emissivity data set available, and P. van Delst for providing the water surface emissivity data set. ECMWF modeled DOD data were obtained from the WMO SDS-WAS NA-ME-E Regional Center (http://sds-was.aemet.es) and from ECMWF (http://apps.ecmwf.int). MODIS and CALIPSO data were downloaded from NASA's EARTHDATA (https://earthdata.nasa.gov/). The IASI LMD data set was downloaded from the ICARE Data and Services Center http://www.icare.univ-lille1.fr/. We thank D. Tanré for the idea of visualizing the regression slopes as in Figure 11. We gratefully acknowledge the entire AERONET network (https://aeronet.gsfc.nasa.gov/), PI's, researchers, and staff for producing and making publicly available their ground-based measurement data. Finally, we thank P. Ginoux and the entire Aerosol-CCI team for useful discussions.

References

ARIA (2017). Aerosol refractive index archive. Retrieved from http://eodg.atm.ox.ac.uk/ARIA/, Accessed: 2017-08-22.

Aires, F., Chédin, A., Scott, N. A., & Rossow, W. B. (2002). A regularized neural net approach for retrieval of atmospheric and surface temperatures with the IASI instrument. *Journal of Applied Meteorology*, *41*(2), 144–159. https://doi.org/10.1175/1520-0450(2002)041<0144:arnnaf>2.0.co;2

Aires, F., Prigent, C., Rossow, W. B., & Rothstein, M. (2001). A new neural network approach including first guess for retrieval of atmospheric water vapor, cloud liquid water path, surface temperature, and emissivities over land from satellite microwave observations. *Journal of Geophysical Research*, *106*(D14), 14,887–14,907. https://doi.org/10.1029/2001JD900085

August, T., Klaes, D., Schlüssel, P., Hultberg, T., Crapeau, M., Arriaga, A., & Calbet, X. (2012). IASI on Metop-A: Operational level 2 retrievals after five years in orbit. *Journal of Quantitative Spectroscopy & Radiative Transfer*, *113*(11), 1340–1371. https://doi.org/10.1016/j.jqsrt.2012.02.028

Aumann, H., Chahine, M., Gautier, C., Goldberg, M., Kalnay, E., McMillin, L., & Susskind, J. (2003). AIRS/AMSU/HSB on the Aqua mission: Design, science objectives, data products, and processing systems. *IEEE Transactions on Geoscience and Remote Sensing*, *41*(2), 253–264. https://doi.org/10.1109/tgrs.2002.808356

Balkanski, Y., Schulz, M., Claquin, T., & Guibert, S. (2007). Reevaluation of mineral aerosol radiative forcings suggests a better agreement with satellite and AERONET data. *Atmospheric Chemistry and Physics*, *7*(1), 81–95. https://doi.org/10.5194/acp-7-81-2007

Bauduin, S., Clarisse, L., Hadji-Lazaro, J., Theys, N., Clerbaux, C., & Coheur, P. F. (2016). Retrieval of near-surface sulfur dioxide (SO_2) concentrations at a global scale using IASI satellite observations. *Atmospheric Measurement Techniques*, *9*(2), 721–740. https://doi.org/10.5194/amt-9-721-2016

Benedetti, A., Morcrette, J. J., Boucher, O., Dethof, A., Engelen, R. J., Fisher, M., & Suttie, M. (2009). Aerosol analysis and forecast in the European Centre for Medium-Range Weather Forecasts Integrated Forecast System: 2. Data assimilation. *Journal of Geophysical Research*, *114*, D13205. https://doi.org/10.1029/2008JD011115

Bi, J., Shi, J., Xie, Y., Liu, Y., Takamura, T., & Khatri, P. (2014). Dust aerosol characteristics and shortwave radiative impact at a Gobi Desert of northwest China during the spring of 2012. *Journal of the Meteorological Society of Japan Ser. II*, *92A*(0), 33–56. https://doi.org/10.2151/jmsj.2014-a03

Blackwell, W., & Chen, F. (2009). *Neural networks in atmospheric remote sensing*. Norwood: Artech House Publishers.

Boucher, O. (2015). *Atmospheric aerosols*. Dordrecht, Netherlands: Springer.

Capelle, V., Chédin, A., Péquignot, E., Schlüssel, P., Newman, S., & Scott, N. (2012). Infrared continental surface emissivity spectra and skin temperature retrieved from IASI observations over the tropics. *Journal of Applied Meteorology and Climatology*, *51*, 1164–1179. https://doi.org/10.1175/JAMC-D-11-0145.1

Capelle, V., Chédin, A., Pondrom, M., Crevoisier, C., Armante, R., Crepeau, L., & Scott, N. (2018). Infrared dust aerosol optical depth retrieved daily from IASI and comparison with AERONET over the period 2007–2016. *Remote Sensing of Environment*, *206*, 15–32. https://doi.org/10.1016/j.rse.2017.12.008

Capelle, V., Chédin, A., Siméon, M., Tsamalis, C., Pierangelo, C., Pondrom, M., & Scott, N. A. (2014). Evaluation of IASI-derived dust aerosol characteristics over the tropical belt. *Atmospheric Chemistry and Physics*, *14*(17), 9343–9362. https://doi.org/10.5194/acp-14-9343-2014

Carboni, E., Thomas, G. E., Sayer, A. M., Siddans, R., Poulsen, C. A., Grainger, R. G., & Veihelmann, B. (2012). Desert dust satellite retrieval intercomparison. *Atmospheric Measurement Techniques*, *5*(1), 1973–2002. https://doi.org/10.5194/amt-5-1973-2012

Chen, S., Huang, J., Qian, Y., Zhao, C., Kang, L., Yang, B., & Zhang, G. (2017). An overview of mineral dust modeling over East Asia. *Journal of Meteorological Research*, *31*(4), 633–653. https://doi.org/10.1007/s13351-017-6142-2

Clarisse, L., Coheur, P. F., Prata, F., Hadji-Lazaro, J., Hurtmans, D., & Clerbaux, C. (2013). A unified approach to infrared aerosol remote sensing and type specification. *Atmospheric Chemistry and Physics*, *13*(4), 2195–2221. https://doi.org/10.5194/acp-13-2195-2013

Clarisse, L., Hurtmans, D., Clerbaux, C., Hadji-Lazaro, J., Ngadi, Y., & Coheur, P. F. (2012). Retrieval of sulphur dioxide from the Infrared Atmospheric Sounding Interferometer (IASI). *Atmospheric Measurement Techniques*, *5*, 581–594. https://doi.org/10.5194/amt-5-581-2012

Clarisse, L., Hurtmans, D., Prata, A. J., Karagulian, F., Clerbaux, C., Mazière, M. D., & Coheur, P. F. (2010). Retrieving radius, concentration, optical depth, and mass of different types of aerosols from high-resolution infrared nadir spectra. *Applied Optics*, *49*(19), 3713–3722. https://doi.org/10.1364/AO.49.003713

Clerbaux, C., Boynard, A., Clarisse, L., George, M., Hadji-Lazaro, J., Herbin, H., & Coheur, P. F. (2009). Monitoring of atmospheric composition using the thermal infrared IASI/MetOp sounder. *Atmospheric Chemistry and Physics*, *9*, 6041–6054. https://doi.org/10.5194/acp-9-6041-2009

Coheur, P. F., Barret, B., Turquety, S., Hurtmans, D., Hadji-Lazaro, J., & Clerbaux, C. (2005). Retrieval and characterization of ozone vertical profiles from a thermal infrared nadir sounder. *Journal of Geophysical Research*, *110*, D24303. https://doi.org/10.1029/2005JD005845

Crevoisier, C., Chédin, A., Matsueda, H., Machida, T., Armante, R., & Scott, N. A. (2009). First year of upper tropospheric integrated content of CO_2 from IASI hyperspectral infrared observations. *Atmospheric Chemistry and Physics*, *9*(14), 4797–4810. https://doi.org/10.5194/acp-9-4797-2009

Crevoisier, C., Clerbaux, C., Guidard, V., Phulpin, T., Armante, R., Barret, B., & Stubenrauch, C. (2014). Towards IASI-New Generation (IASI-NG): Impact of improved spectral resolution and radiometric noise on the retrieval of thermodynamic, chemistry and climate variables. *Atmospheric Measurement Techniques*, *7*(12), 4367–4385. https://doi.org/10.5194/amt-7-4367-2014

Cuesta, J., Eremenko, M., Flamant, C., Dufour, G., Laurent, B., Bergametti, G., & Zhou, D. (2015). Three-dimensional distribution of a major desert dust outbreak over East Asia in March 2008 derived from IASI satellite observations. *Journal of Geophysical Research: Atmospheres*, *120*, 7099–7127. https://doi.org/10.1002/2014jd022406

Cuevas, E., Camino, C., Benedetti, A., Basart, S., Terradellas, E., Baldasano, J. M., & Schulz, M. (2015). The MACC-II 2007–2008 reanalysis: Atmospheric dust evaluation and characterization over northern Africa and the Middle East. *Atmospheric Chemistry and Physics*, *15*(8), 3991–4024. https://doi.org/10.5194/acp-15-3991-2015

D'Almeida, G., Koepke, P., & Shettle, E. (1991). *Atmospheric aerosols. Global climatology and radiative characteristics*. Hampton, VA: A. DEEPAK Publishing.

DeSouza-Machado, S., Strow, L., Hannon, S., & Motteler, H. (2006). Infrared dust spectral signatures from AIRS. *Geophysical Research Letters*, *33*, L03801. https://doi.org/10.1029/2005GL024364

DeSouza-Machado, S. G., Strow, L. L., Imbiriba, B., McCann, K. K., Hoff, R. M., Hannon, S. E., & Torres, O. (2010). Infrared retrievals of dust using AIRS: Comparisons of optical depths and heights derived for a North African dust storm to other collocated EOS A-Train and surface observations. *Journal of Geophysical Research*, *115*, D15201. https://doi.org/10.1029/2009JD012842

Dee, D. P., Uppala, S. M., Simmons, A. J., Berrisford, P., Poli, P., Kobayashi, S., & Vitart, F. (2011). The ERA-Interim reanalysis: Configuration and performance of the data assimilation system. *Quarterly Journal of the Royal Meteorological Society*, *137*(656), 553–597. https://doi.org/10.1002/qj.828

Di Biagio, C., Boucher, H., Caquineau, S., Chevaillier, S., Cuesta, J., & Formenti, P. (2014). Variability of the infrared complex refractive index of African mineral dust: Experimental estimation and implications for radiative transfer and satellite remote sensing. *Atmospheric Chemistry and Physics*, *14*(20), 11,093–11,116. https://doi.org/10.5194/acp-14-11093-2014

Di Biagio, C., Formenti, P., Balkanski, Y., Caponi, L., Cazaunau, M., Pangui, E., & Doussin, J. F. (2017). Global scale variability of the mineral dust long-wave refractive index: A new dataset of in situ measurements for climate modeling and remote sensing. *Atmospheric Chemistry and Physics*, *17*(3), 1901–1929. https://doi.org/10.5194/acp-17-1901-2017

Di Biagio, C., Formenti, P., Styler, S. A., Pangui, E., & Doussin, J. F. (2014). Laboratory chamber measurements of the longwave extinction spectra and complex refractive indices of African and Asian mineral dusts. *Geophysical Research Letters*, *41*, 6289–6297. https://doi.org/10.1002/2014GL060213

Evan, A. T., Flamant, C., Gaetani, M., & Guichard, F. (2016). The past, present and future of African dust. *Nature*, *531*(7595), 493–495. https://doi.org/10.1038/nature17149

Fischer, K. (1976). The optical constants of atmospheric aerosol particles in the 7.5–12 μm spectral region. *Tellus*, *28*(3), 266–274. https://doi.org/10.1111/j.2153-3490.1976.tb00675.x

Flemming, J., Benedetti, A., Inness, A., Engelen, R. J., Jones, L., Huijnen, V., & Katragkou, E. (2017). The CAMS interim reanalysis of carbon monoxide, ozone and aerosol for 2003–2015. *Atmospheric Chemistry and Physics*, *17*(3), 1945–1983. https://doi.org/10.5194/acp-17-1945-2017

Fouquart, Y., Bonnel, B., Brogniez, G., Buriez, J., Smith, L., & Morcrette, J. (1987). Observations of Saharan aerosols: Results of ECLATS field experiment. Part II: Broadband radiative characteristics of the aerosols and vertical radiative flux divergence. *Journal of Applied Meteorology and Climatology*, *26*, 38–52. https://doi.org/10.1175/1520-0450(1987)026<0038:OOSARO>2.0.CO;2

Fouquart, Y., Bonnel, B., Brogniez, G., Cerf, A., Chaoui, M., Smith, L., & Vanhoutte, J. C. (1984). In H E. Gerber & A. Deepak (Eds.), *Size distribution and optical properties of Saharan aerosols during ECLATS, Aerosols and their climatic effects* (pp. 35–62). Hampton, VA.

Gehlot, S., Minnett, P. J., & Stammer, D. (2015). Impact of Sahara dust on solar radiation at Cape Verde Islands derived from MODIS and surface measurements. *Remote Sensing of Environment*, *166*, 154–162. https://doi.org/10.1016/j.rse.2015.05.026

Giglio, L., Csiszar, I., & Justice, C. O. (2006). Global distribution and seasonality of active fires as observed with the Terra and Aqua Moderate Resolution Imaging Spectroradiometer (MODIS) sensors. *Journal of Geophysical Research*, *111*, G02016. https://doi.org/10.1029/2005JG000142

Ginoux, P., Prospero, J. M., Gill, T. E., Hsu, N. C., & Zhao, M. (2012). Global-scale attribution of anthropogenic and natural dust sources and their emission rates based on MODIS Deep Blue aerosol products. *Reviews of Geophysics*, *50*, RG3005. https://doi.org/10.1029/2012RG000388

Guirado, C., Cuevas, E., Cachorro, V. E., Toledano, C., Alonso-Pérez, S., Bustos, J. J., & de Frutos, A. M. (2014). Aerosol characterization at the Saharan AERONET site Tamanrasset. *Atmospheric Chemistry and Physics*, *14*(21), 11,753–11,773. https://doi.org/10.5194/acp-14-11753-2014

Hadji-Lazaro, J., Clerbaux, C., & Thiria, S. (1999). An inversion algorithm using neural networks to retrieve atmospheric CO total columns from high-resolution nadir radiances. *Journal of Geophysical Research*, *104*(D19), 23,841–23,854. https://doi.org/10.1029/1999JD900431

Han, H. J., Sohn, B. J., Huang, H. L., Weisz, E., Saunders, R., & Takamura, T. (2012). An improved radiance simulation for hyperspectral infrared remote sensing of Asian dust. *Journal of Geophysical Research*, *117*, D09211. https://doi.org/10.1029/2012JD017466

Hess, M., Koepke, P., & Schult, I. (1998). Optical properties of aerosols and clouds: The software package OPAC. *Bulletin of the American Meteorological Society*, *79*(5), 831–844. https://doi.org/10.1175/1520-0477(1998)079<0831:OPOAAC>2.0.CO;2

Highwood, E., Haywood, J., Silverstone, M., Newman, S. M., & Taylor, J. (2003). Radiative properties and direct effect of Saharan dust measured by the C-130 aircraft during Saharan Dust Experiment (SHADE): 2. Terrestrial spectrum. *Journal of Geophysical Research*, *108*(D18), 8578. https://doi.org/10.1029/2002JD002552

Holben, B. N., Tanré, D., Smirnov, A., Eck, T. F., Slutsker, I., Abuhassan, N., & Zibordi, G. (2001). An emerging ground-based aerosol climatology: Aerosol optical depth from AERONET. *Journal of Geophysical Research*, *106*(D11), 12,067–12,097. https://doi.org/10.1029/2001JD900014

Huang, J., Guo, J., Wang, F., Liu, Z., Jeong, M. J., Yu, H., & Zhang, Z. (2015). CALIPSO inferred most probable heights of global dust and smoke layers. *Journal of Geophysical Research: Atmospheres*, *120*, 5085–5100. https://doi.org/10.1002/2014jd022898

Inness, A., Baier, F., Benedetti, A., Bouarar, I., Chabrillat, S., Clark, H., & the MACC team (2013). The MACC reanalysis: An 8 yr data set of atmospheric composition. *Atmospheric Chemistry and Physics*, *13*(8), 4073–4109. https://doi.org/10.5194/acp-13-4073-2013

Ioannou, I., Gilerson, A., Gross, B., Moshary, F., & Ahmed, S. (2011). Neural network approach to retrieve the inherent optical properties of the ocean from observations of MODIS. *Applied Optics*, *50*(19), 3168. https://doi.org/10.1364/ao.50.003168

Jacquinet-Husson, N., Armante, R., Scott, N., Chédin, A., Crépeau, L., Boutammine, C., & Makie, A. (2016). The 2015 edition of the GEISA spectroscopic database. *Journal of Molecular Spectroscopy*, *327*, 31–72. https://doi.org/10.1016/j.jms.2016.06.007

Klüser, L., Kleiber, P., Holzer-Popp, T., & Grassian, V. (2012). Desert dust observation from space—Application of measured mineral component infrared extinction spectra. *Atmospheric Environment*, *54*, 419–427. https://doi.org/10.1016/j.atmosenv.2012.02.011

Klüser, L., Martynenko, D., & Holzer-Popp, T. (2011). Thermal infrared remote sensing of mineral dust over land and ocean: A spectral SVD based retrieval approach for IASI. *Atmospheric Measurement Techniques*, *4*(5), 757–773. https://doi.org/10.5194/amt-4-757-2011

Knippertz, P., & Stuut, J. BW. (2014). *Mineral dust. A key player in the Earth system*. Springer.

Knippertz, P., & Todd, M. C. (2012). Mineral dust aerosols over the Sahara: Meteorological controls on emission and transport and implications for modeling. *Reviews of Geophysics*, *50*, RG1007. https://doi.org/10.1029/2011RG000362

Koepke, P., Hess, M., Schult, I., & Shettle, E. (1997). Global Aerosol Data Set No. 243, Hamburg, Max-Planck-Institut für Meteorologie.

Levy, R., Leptoukh, G., Kahn, R., Zubko, V., Gopalan, A., & Remer, L. (2009). A critical look at deriving monthly aerosol optical depth from satellite data. *IEEE Transactions on Geoscience and Remote Sensing*, *47*(8), 2942–2956. https://doi.org/10.1109/tgrs.2009.2013842

Levy, R. C., Mattoo, S., Munchak, L. A., Remer, L. A., Sayer, A. M., Patadia, F., & Hsu, N. C. (2013). The Collection 6 MODIS aerosol products over land and ocean. *Atmospheric Measurement Techniques*, *6*(11), 2989–3034. https://doi.org/10.5194/amt-6-2989-2013

Levy, R. C., Remer, L. A., Mattoo, S., Vermote, E. F., & Kaufman, Y. J. (2007). Second-generation operational algorithm: Retrieval of aerosol properties over land from inversion of Moderate Resolution Imaging Spectroradiometer spectral reflectance. *Journal of Geophysical Research*, *112*, D13211. https://doi.org/10.1029/2006JD007811

Liuzzi, G., Masiello, G., Serio, C., Meloni, D., Biagio, C. D., & Formenti, P. (2017). Consistency of dimensional distributions and refractive indices of desert dust measured over Lampedusa with IASI radiances. *Atmospheric Measurement Techniques*, *10*(2), 599–615. https://doi.org/10.5194/amt-10-599-2017

Longtin, D. R. (1988). A wind dependent desert aerosol model: Radiative properties, United States Air Force, Air Force Systems Command, Air Force Geophysics Laboratory, AFGL-TR-88-0112.
Mahowald, N., Albani, S., Kok, J. F., Engelstaeder, S., Scanza, R., Ward, D. S., & Flanner, M. G. (2014). The size distribution of desert dust aerosols and its impact on the Earth system. *Aeolian Research*, *15*, 53–71. https://doi.org/10.1016/j.aeolia.2013.09.002
Massie, S., & Hervig, M. (2013). HITRAN 2012 refractive indices. *Journal of Quantitative Spectroscopy & Radiative Transfer*, *130*, 373–380. https://doi.org/10.1016/j.jqsrt.2013.06.022
Masuda, K., Takashima, T., & Takayama, Y. (1988). Emissivity of pure and sea waters for the model sea surface in the infrared window regions. *Remote Sensing of Environment*, *24*(2), 313–329. https://doi.org/10.1016/0034-4257(88)90032-6
Mitchell, R. M., Forgan, B. W., & Campbell, S. K. (2017). The climatology of Australian aerosol. *Atmospheric Chemistry and Physics*, *17*(8), 5131–5154. https://doi.org/10.5194/acp-17-5131-2017
Mona, L., Amodeo, A., Pandolfi, M., & Pappalardo, G. (2006). Saharan dust intrusions in the Mediterranean area: Three years of Raman lidar measurements. *Journal of Geophysical Research*, *111*, D16203. https://doi.org/10.1029/2005JD006569
Morcrette, J. J., Boucher, O., Jones, L., Salmond, D., Bechtold, P., Beljaars, A., & Untch, A. (2009). Aerosol analysis and forecast in the European Centre for Medium-Range Weather Forecasts Integrated Forecast System: Forward modeling. *Journal of Geophysical Research*, *114*, D06206. https://doi.org/10.1029/2008JD011235
Moxnes, E. D., Kristiansen, N. I., Stohl, A., Clarisse, L., Durant, A., Weber, K., & Vogel, A. (2014). Separation of ash and sulfur dioxide during the 2011 Grímsvötn eruption. *Journal of Geophysical Research: Atmospheres*, *119*, 7477–7501. https://doi.org/10.1002/2013JD021129
Nalli, N., Minnett, P., & van Delst, P. (2008). Emissivity and reflection model for calculating unpolarized isotropic water surface-leaving radiance in the infrared. I: Theoretical development and calculations. *Applied Optics*, *47*(21), 3701–3721. https://doi.org/10.1364/AO.47.004649
Newman, S. M., Clarisse, L., Hurtmans, D., Marenco, F., Johnson, B., Turnbull, K., & Haywood, J. (2012). A case study of observations of volcanic ash from the Eyjafjallajökull eruption: 2. Airborne and satellite radiative measurements. *Journal of Geophysical Research*, *117*, D00U13. https://doi.org/10.1029/2011JD016780
Newman, S. M., Smith, J. A., Glew, M. D., Rogers, S. M., & Taylor, JP. (2005). Temperature and salinity dependence of sea surface emissivity in the thermal infrared. *Quarterly Journal of the Royal Meteorological Society*, *131*(610), 2539–2557. https://doi.org/10.1256/qj.04.150
Noia, A. D., & Hasekamp, O. P. (2018). *Neural networks and support vector machines and their application to aerosol and cloud remote sensing: A review*, Springer series in light scattering (pp. 279–329). Springer International Publishing. https://doi.org/10.1007/978-3-319-70796-9_4
O'Neill, N. T., Eck, T. F., Smirnov, A., Holben, B. N., & Thulasiraman, S. (2003). Spectral discrimination of coarse and fine mode optical depth. *Journal of Geophysical Research*, *108*(D17), 4559. https://doi.org/10.1029/2002JD002975
Patterson, E. M. (1981). Optical properties of the crustal aerosol: Relation to chemical and physical characteristics. *Journal of Geophysical Research*, *86*, 3236–3246. https://doi.org/10.1029/JC086iC04p03236
Peyridieu, S., Chédin, A., Capelle, V., Tsamalis, C., Pierangelo, C., Armante, R., & Scott, N. A. (2013). Characterisation of dust aerosols in the infrared from IASI and comparison with PARASOL, MODIS, MISR, CALIOP, and AERONET observations. *Atmospheric Chemistry and Physics*, *13*(12), 6065–6082. https://doi.org/10.5194/acp-13-6065-2013
Peyridieu, S., Chédin, A., Tanré, D., Capelle, V., Pierangelo, C., Lamquin, N., & Armante, R. (2010). Saharan dust infrared optical depth and altitude retrieved from AIRS: A focus over North Atlantic - comparison to MODIS and CALIPSO. *Atmospheric Chemistry and Physics*, *10*, 1953–1967. https://doi.org/10.5194/acp-10-1953-2010
Pierangelo, C., Chedin, A., Heilliette, S., Jacquinet-Husson, N., & Armante, R. (2004). Dust altitude and infrared optical depth from AIRS. *Atmospheric Chemistry and Physics*, *4*, 1813–1822. https://doi.org/10.5194/acp-4-1813-2004
Pierangelo, C., Mishchenko, M., Balkanski, Y., & Chedin, A. (2005). Retrieving the effective radius of Saharan dust coarse mode from AIRS. *Geophysical Research Letters*, *32*, L20813. https://doi.org/10.1029/2005GL023425
Pinker, R. T., Liu, H., Osborne, S. R., & Akoshile, C. (2010). Radiative effects of aerosols in sub-Sahel Africa: Dust and biomass burning. *Journal of Geophysical Research*, *115*, D15205. https://doi.org/10.1029/2009JD013335
Platnick, S., et al. (2017). MODIS Atmosphere L3 Monthly Product. NASA MODIS Adaptive Procesing System, Goddard Space Flight Center, USA. https://doi.org/10.5067/MODIS/MOD08_M3.061
Pollack, J., Toon, O., & Khare, B. (1973). Optical properties of some terrestrial rocks and glasses. *Icarus*, *19*, 372–389. https://doi.org/10.1016/0019-1035(73)90115-2
Popp, T., de Leeuw, G., Bingen, C., Brhl, C., Capelle, V., Chedin, A., & Xue, Y. (2016). Development, production and evaluation of aerosol climate data records from European satellite observations (Aerosol_cci). *Remote Sensing*, *8*(5), 421. https://doi.org/10.3390/rs8050421
Prospero, J. M., & Mayol-Bracero, O. L. (2013). Understanding the transport and impact of African dust on the Caribbean Basin. *Bulletin of the American Meteorological Society*, *94*(9), 1329–1337. https://doi.org/10.1175/bams-d-12-00142.1
Querry, M. (1987). Optical constants of minerals and other materials from the millimeter to the ultraviolet, University of Missouri-Kansas city, Report CRDEC-CR-88009.
Reid, J., Jonsson, H., Maring, H., Smirnov, A., Savoie, D. L., Cliff, S., & Tsay, S. C. (2003). Comparison of size and morphological measurements of coarse mode dust particles from Africa. *Journal of Geophysical Research*, *108*(D19), 8593. https://doi.org/10.1029/2002JD002485
Ridley, D. A., Heald, C. L., & Ford, B. (2012). North African dust export and deposition: A satellite and model perspective. *Journal of Geophysical Research*, *117*, D02202. https://doi.org/10.1029/2011JD016794
Sayer, A. M., Hsu, N. C., Bettenhausen, C., & Jeong, M. J. (2013). Validation and uncertainty estimates for MODIS Collection 6 "Deep Blue" aerosol data. *Journal of Geophysical Research: Atmospheres*, *118*, 7864–7872. https://doi.org/10.1002/jgrd.50600
Sayer, A. M., Munchak, L. A., Hsu, N. C., Levy, R. C., Bettenhausen, C., & Jeong, M. J. (2014). MODIS Collection 6 aerosol products: Comparison between Aqua's e-Deep Blue, Dark Target, and 'merged' data sets, and usage recommendations. *Journal of Geophysical Research: Atmospheres*, *119*, 13,965–13,989. https://doi.org/10.1002/2014JD022453
Schepanski, K., Tegen, I., Todd, M. C., Heinold, B., Bnisch, G., Laurent, B., & Macke, A. (2009). Meteorological processes forcing Saharan dust emission inferred from MSG-SEVIRI observations of subdaily dust source activation and numerical models. *Journal of Geophysical Research*, *114*, D10201. https://doi.org/10.1029/2008JD010325
Schutgens, N., Tsyro, S., Gryspeerdt, E., Goto, D., Weigum, N., Schulz, M., & Stier, P. (2017). On the spatio-temporal representativeness of observations. *Atmospheric Chemistry and Physics*, *17*(16), 9761–9780. https://doi.org/10.5194/acp-17-9761-2017
Seemann, S. W., Borbas, EE., Knuteson, RO., Stephenson, GR., & Huang, H. L. (2008). Development of a global infrared land surface emissivity database for application to clear sky sounding retrievals from multispectral satellite radiance measurements. *Journal of Applied Meteorology and Climatology*, *47*(1), 108–123. https://doi.org/10.1175/2007JAMC1590.1
Shettle, E., & Fenn, R. (1979). Models for the aerosols of the lower atmosphere and the effects of humidity variations on their optical properties, United States Air Force, Air Force Systems Command, Air Force Geophysics Laboratory, AFGL-TR-79-0214.

Smirnov, A., Holben, B. N., Eck, T. F., Slutsker, I., Chatenet, B., & Pinker, R. T. (2002). Diurnal variability of aerosol optical depth observed at AERONET (Aerosol Robotic Network) sites. *Geophysical Research Letters*, *29*(23), 2115. https://doi.org/10.1029/2002GL016305

Sokolik, I., Andronova, A., & Johnson, T. C. (1993). Complex refractive index of atmospheric dust aerosols. *Atmospheric Environment*, *27*(16), 2495–2502. https://doi.org/10.1016/0960-1686(93)90021-P

Sokolik, I. N., Toon, O. B., & Bergstrom, R. W. (1998). Modeling the radiative characteristics of airborne mineral aerosols at infrared wavelengths. *Journal of Geophysical Research*, *103*, 8813–8826. https://doi.org/10.1029/98JD00049

Spada, M., Jorba, O., García-Pando, C. P., Janjic, Z., & Baldasano, J. M. (2013). Modeling and evaluation of the global sea-salt aerosol distribution: Sensitivity to size-resolved and sea-surface temperature dependent emission schemes. *Atmospheric Chemistry and Physics*, *13*(23), 11,735–11,755. https://doi.org/10.5194/acp-13-11735-2013

Sun, K., Zhu, L., Cady-Pereira, K., Miller, C. C., Chance, K., Clarisse, L., & Zondlo, M. (2018). A physics-based approach to oversample multi-satellite, multi-species observations to a common grid. *Atmospheric Measurement Techniques Discuss*, *11*, 6679–6701. https://doi.org/10.5194/amt-2018-253

Tanré, D., Bréon, FM., Deuzé, JL., Dubovik, O., Ducos, F., François, P., & Waquet, F. (2011). Remote sensing of aerosols by using polarized, directional and spectral measurements within the A-Train: The PARASOL mission. *Atmospheric Measurement Techniques*, *4*(7), 1383–1395. https://doi.org/10.5194/amt-4-1383-2011

Taylor, M., Kazadzis, S., Tsekeri, A., Gkikas, A., & Amiridis, V. (2014). Satellite retrieval of aerosol microphysical and optical parameters using neural networks: A new methodology applied to the Sahara desert dust peak. *Atmospheric Measurement Techniques*, *7*(9), 3151–3175. https://doi.org/10.5194/amt-7-3151-2014

Tsamalis, C., Chédin, A., Pelon, J., & Capelle, V. (2013). The seasonal vertical distribution of the Saharan air layer and its modulation by the wind. *Atmospheric Chemistry and Physics*, *13*(22), 11,235–11,257. https://doi.org/10.5194/acp-13-11235-2013

Van Damme, M., Clarisse, L., Heald, C., Hurtmans, D., Ngadi, Y., Clerbaux, C., & Coheur, P. (2014). Global distributions, time series and error characterization of atmospheric ammonia (NH_3) from IASI satellite observations. *Atmospheric Chemistry and Physics*, *14*(6), 2905–2922. https://doi.org/10.5194/acp-14-2905-2014

Van Damme, M., Whitburn, S., Clarisse, L., Clerbaux, C., Hurtmans, D., & Coheur, P. F. (2017). Version 2 of the IASI NH_3 neural network retrieval algorithm: Near-real-time and reanalysed datasets. *Atmospheric Measurement Techniques*, *10*(12), 4905–4914. https://doi.org/10.5194/amt-10-4905-2017

Vandenbussche, S., Kochenova, S., Vandaele, A. C., Kumps, N., & De Mazière, M. (2013). Retrieval of desert dust aerosol vertical profiles from IASI measurements in the TIR atmospheric window. *Atmospheric Measurement Techniques*, *6*(10), 2577–2591. https://doi.org/10.5194/amt-6-2577-2013

Varga, G. (2012). Spatio-temporal distribution of dust storms—A global coverage using NASA TOMS aerosol measurements. *Hungarian Geographical Bulletin*, *61*(4), 275–298.

Varga, G., & Szalai, Z. (2013). Geographical distribution and geomorphological characteristics of major global dust source areas. Talajpusztuls trben s idben (az "erzis kerekasztal 2013" kzlemnyei) (pp. 40–46). Kocsis Kroly MTA CSFK Fldrajztudomnyi Intzet Igazgat.

Ventress, LJ., McGarragh, G., Carboni, E., Smith, AJ., & Grainger, RG. (2016). Retrieval of ash properties from IASI measurements. *Atmospheric Measurement Techniques*, *9*(11), 5407–5422. https://doi.org/10.5194/amt-9-5407-2016

Verma, S., Payra, S., Gautam, R., Prakash, D., Soni, M., Holben, B., & Bell, S. (2013). Dust events and their influence on aerosol optical properties over Jaipur in northwestern India. *Environmental Monitoring and Assessment*, *185*(9), 7327–7342. https://doi.org/10.1007/s10661-013-3103-9

Volz, F. (1972a). Infrared absorption by atmospheric aerosol substances. *Journal of Geophysical Research*, *77*, 1017–1031. https://doi.org/10.1029/JC077i006p01017

Volz, F. (1972b). Infrared refractive index of atmospheric aerosol substances. *Applied Optics*, *11*, 755–759. https://doi.org/10.1364/AO.11.000755

Volz, F. (1973). Infrared optical constants of ammonium sulfate, Sahara dust; volcanic pumice and flyash. *Applied Optics*, *12*, 564–568. https://doi.org/10.1364/AO.12.000564

Volz, F. (1983). Infrared optical constants of aerosols at some locations. *Applied Optics*, *22*(23), 3690–3700. https://doi.org/10.1364/AO.22.003690

Walker, J. C., Dudhia, A., & Carboni, E. (2011). An effective method for the detection of trace species demonstrated using the MetOp Infrared Atmospheric Sounding Interferometer. *Atmospheric Measurement Techniques*, *4*(5), 1567–1580. https://doi.org/10.5194/amt-4-1567-2011

Wang, J., Xia, X., Wang, P., & Christopher, S. A. (2004). Diurnal variability of dust aerosol optical thickness and (Ångström exponent over dust source regions in China. *Geophysical Research Letters*, *31*, L08107. https://doi.org/10.1029/2004GL019580

Washington, R., Bouet, C., Cautenet, G., Mackenzie, E., Ashpole, I., Engelstaedter, S., & Tegen, I. (2009). Dust as a tipping element: The Bodélé Depression, Chad. *Proceedings of the National Academy of Sciences*, *106*(49), 20,564–20,571. https://doi.org/10.1073/pnas.0711850106

Whitburn, S., Damme, M. V., Clarisse, L., Bauduin, S., Heald, C. L., Hadji-Lazaro, J., & Coheur, P. F. (2016). A flexible and robust neural network IASI-NH_3 retrieval algorithm. *Journal of Geophysical Research: Atmospheres*, *121*, 6581–6599. https://doi.org/10.1002/2016jd024828

Winker, D. (2016). CALIPSO LID_L2_05kmALay-Standard HDF file-version 4.10. Retrieved from https://doi.org/10.5067/caliop/calipso/lid_l2_05kmalay-standard-v4-10

Winker, DM., Tackett, JL., Getzewich, BJ., Liu, Z., Vaughan, MA., & Rogers, RR. (2013). The global 3-D distribution of tropospheric aerosols as characterized by CALIOP. *Atmospheric Chemistry and Physics*, *13*(6), 3345–3361. https://doi.org/10.5194/acp-13-3345-2013

Winker, D. M., Vaughan, M. A., Omar, A., Hu, Y., Powell, K. A., Liu, Z., & Young, S. A. (2009). Overview of the CALIPSO mission and CALIOP data processing algorithms. *Journal of Atmospheric and Oceanic Technology*, *26*(11), 2310–2323. https://doi.org/10.1175/2009JTECHA1281.1

World Meteorological Organization (1986). A preliminary cloudless standard atmosphere for radiation computation, WCP-112, Boulder, Colorado, World Climate Research Program, CAS, Radiation Commission of IAMAP.

Xi, X., & Sokolik, I. N. (2015). Dust interannual variability and trend in central Asia from 2000 to 2014 and their climatic linkages. *Journal of Geophysical Research: Atmospheres*, *120*, 12,175–12,197. https://doi.org/10.1002/2015jd024092

Xia, X., Chen, H., Goloub, P., Zong, X., Zhang, W., & Wang, P. (2013). Climatological aspects of aerosol optical properties in North China Plain based on ground and satellite remote-sensing data. *Journal of Quantitative Spectroscopy & Radiative Transfer*, *127*, 12–23. https://doi.org/10.1016/j.jqsrt.2013.06.024

Yao, Z., Li, J., Han, H. J., Huang, A., Sohn, B. J., & Zhang, P. (2012). Asian dust height and infrared optical depth retrievals over land from hyperspectral longwave infrared radiances. *Journal of Geophysical Research*, *117*, D19202. https://doi.org/10.1029/2012JD017799

Yu, H., Chin, M., Winker, D. M., Omar, A. H., Liu, Z., Kittaka, C., & Diehl, T. (2010). Global view of aerosol vertical distributions from CALIPSO lidar measurements and GOCART simulations: Regional and seasonal variations. *Journal of Geophysical Research*, *115*, D00H30. https://doi.org/10.1029/2009JD013364

Yu, H., Remer, L. A., Kahn, R. A., Chin, M., & Zhang, Y. (2013). Satellite perspective of aerosol intercontinental transport: From qualitative tracking to quantitative characterization. *Atmospheric Research*, *124*, 73–100. https://doi.org/10.1016/j.atmosres.2012.12.013

Zhang, J., & Reid, J. S. (2010). A decadal regional and global trend analysis of the aerosol optical depth using a data-assimilation grade over-water MODIS and level 2 MISR aerosol products. *Atmospheric Chemistry and Physics*, *10*(22), 10,949–10,963. https://doi.org/10.5194/acp-10-10949-2010

Zhou, D. K., Larar, A. M., & Liu, X. (2013). MetOp-A/IASI observed continental thermal IR emissivity variations. *IEEE Journal of Selected Topics in Applied Earth Observations Remote Sensing*, *6*(3), 1156–1162. https://doi.org/10.1109/JSTARS.2013.2238892

Zhou, D., Larar, A., Liu, X., Smith, W., Strow, L., Yang, P., & Calbet, X. (2011). Global land surface emissivity retrieved from satellite ultraspectral IR measurements. *IEEE Transactions on Geoscience and Remote Sensing*, *49*, 1277–1290. https://doi.org/10.1109/TGRS.2010.2051036